



UNIVERSIDADE FEDERAL DO CEARÁ
CENTRO DE TECNOLOGIA
DEPARTAMENTO DE ENGENHARIA DE TELEINFORMÁTICA
CURSO DE GRADUAÇÃO EM ENGENHARIA DE TELECOMUNICAÇÕES

LUCAS DE SOUZA ABDALAH

NONINVASIVE ASSESSMENT OF ATRIAL FIBRILLATION
COMPLEXITY USING TENSOR DECOMPOSITION TECHNIQUES

FORTALEZA – CE
2022

Dedico este trabalho aos meus pais.

AGRADECIMENTOS

Em primeiro lugar, aos meus pais, por todo o apoio e pela ajuda, que muito contribuíram para a realização deste trabalho.

Aos meus professores e orientadores, em especial a Walter Freitas Jr., Vicente Zarzoso e Pedro Marinho.

Aos meus amigos e aos colegas de universidade, que sempre estiveram ao meu lado, pela amizade incondicional e pelo apoio demonstrado ao longo de todo o período de tempo em que me dediquei a este trabalho, em especial a Yvo Menezes, Kenneth Brenner, Alyson Veras, Melyssa Diniz, Arthur Anderson e Endley Alves.

Aos meus companheiros de diretório acadêmico e de PET, por todo o apoio e pela ajuda, que muito contribuíram para a realização deste trabalho.

Aos meus companheiros da música, que me incentivaram nos momentos difíceis e compreenderam a minha ausência enquanto eu me dedicava à realização deste trabalho, em especial a Miguel Abdala.

Aos funcionários e às funcionárias do Departamento de Engenharia de Teleinformática, em especial a Cleiton, Miraneide, Oriel, Cindy, Anagildo.

O presente trabalho foi realizado com apoio da Coordenação de Aperfeiçoamento de Pessoal de Nível Superior Brasil (CAPES) - Código de Financiamento 001.

“Toute réussite déguise une abdication.”
Simone de Beauvoir (1958)

RESUMO

Acredita-se que seja responsável por um quarto dos acidentes vasculares cerebrais, a fibrilação atrial (FA) é a arritmia cardíaca mais comum encontrada na prática clínica. A FA persistente é um caso complexo dessa arritmia caracterizada por ativação cardíaca descoordenada e irregular. Embora a ablação por cateter seja cada vez mais usada dado suas baixas taxas de recorrência em comparação a outras opções de tratamento, protocolos de intervenção confiáveis adotados por toda a comunidade ritmológica ainda não foram encontrados. A fim de orientar as intervenções e melhorar sua taxa de sucesso, reduzindo sua duração e risco de complicações, as técnicas de análise do sinal cardíaco baseadas no eletrocardiograma (ECG) de superfície são muito interessantes devido ao seu baixo custo e sua natureza não invasiva. No entanto, apesar do crescente interesse em metodologias não invasivas para avaliar a complexidade do sinal de FA persistente, seu desempenho ainda é limitado. Para preencher essas lacunas, o presente trabalho utiliza o potencial das técnicas de decomposições tensoriais para avaliar a complexidade dos sinais de ECG durante o procedimento de ablação por cateter para o tratamento de FA. As decomposições de tensores são uma ferramenta de análise de dados cada vez mais usada no processamento de sinais, entretanto só foram recentemente aplicadas no contexto da análise de sinais de FA. O algoritmo *Coinstrained Alternating Group Lasso* (CAGL), recém desenvolvido para o cálculo da decomposição tensorial em blocos de termos (*block term decomposition*, BTD) permite a estimativa simultânea dos parâmetros do modelo (posto e número de blocos), o que possibilita a sua proposição como ferramenta de avaliação da complexidade do sinal de FA usando parâmetros do modelo, como o posto dos blocos estimados como fonte deste sinal. A abordagem provém uma solução original e promissora, resultando em artigo publicado na conferência *Computing in Cardiology* (Rimni, Itália, 13-16 set 2020), sendo sugerida para auxiliar ritmologistas no procedimento de ablação às especificidades de cada paciente, com as devidas adaptações necessárias.

Palavras-chave: Decomposições Tensoriais, Eletrocardiograma, Fibrilação Atrial, Separação Cega de Fontes.

ABSTRACT

Believed to be responsible for a quarter of brain strokes, atrial fibrillation (AF) is the most common cardiac arrhythmia encountered in clinical practice. Persistent AF is a complex case of this arrhythmia characterized by uncoordinated and irregular cardiac activation. Stepwise catheter ablation is increasingly used because of its low recurrence rates compared to other treatment options, but reliable intervention protocols adopted by the whole rhythmic community are still to be proposed. In order to guide interventions and improve their success rate while reducing their duration and risk of complications, cardiac signal analysis techniques based on the surface electrocardiogram (ECG) are of great interest due to their low cost and their non-invasive character. However, despite the growing interest in non-invasive methodologies for assessing the complexity of the persistent AF signal, their performance is still limited. To fill these gaps, this work aimed to take advantage on the power of tensor decomposition techniques to assess the complexity of ECG signals the catheter ablation procedure during AF treatment. Tensor decompositions are increasingly used data analysis tools in signal processing, but they have only recently been applied to AF signal analysis. The Constrained Alternating Group Lasso (CAGL) algorithm has just been developed for the calculation of the block term tensor decomposition (BTD) and it allows the simultaneous estimation of the model parameters (rank and number of blocks). In order to evaluate the clinical significance of the tensor characterization, the present work used the CAGL algorithm, with the necessary adaptations, to evaluate the complexity of the AF signal based on the BTD model parameters, such as the rank of the matrices of the signal source estimated blocks. This approach provided an original and promising solution, which resulted in an article published in the *Computing in Cardiology* conference (Rimini, Italy, sep. 13-16), which can allow rhythmologists to better tailor ablation interventions to the specificities of each patient.

Keywords: Atrial Fibrillation, Blind Source Separation, Electrocardiogram, Tensor Decompositions.

LIST OF FIGURES

Figure 1 – Heart’s structure.	5
Figure 2 – Heartbeat sequence present in Lead V5 from a standard 12-lead ECG, without a frame.	6
Figure 3 – Single Heartbeat representation in Lead V5 from a standard 12-lead ECG. .	6
Figure 4 – Catheter ablation procedure.	8
Figure 5 – Node diagram of a simple BSS model.	10
Figure 6 – Visual representation of a Hankel matrix \mathbf{H}_s built from a signal $s(n)$. .	11
Figure 7 – The block term decomposition $(L_r, L_r, 1)$ representation of an arbitrary third-order tensor.	13
Figure 8 – Tensor representation: each lead mapped into a Hankel matrix and stacked on its third mode.	15
Figure 9 – Trend over Empirical CDF’s of NMSE over estimated blocks attained by AGL and BTD-GN for 500 realizations of a noise random BTD model (SNR = 20dB).	20
Figure 10 – The ECDF of NMSE in the case AGL(3,6), varying both the region used on the γ -sweeping procedure and the proximal term τ . The lower triangles indicate γ_0 ’s ECDF, while the upper triangles represent the last iteration. The gray curves are intermediaries iterations.	22
Figure 11 – Signal that mimics AA.	24
Figure 12 – Semi-synthetic signal for lead V1 from equation (28) model after down-sampling.	25
Figure 13 – Number of blocks estimation for each γ in five CAGL runs.	27
Figure 14 – Semi-synthetic ECG single sided frequency spectrum (Welch’s method). .	27
Figure 15 – Example of AA block source with: SC = 63.5%, DF = 6.2 Hz, and kurtosis = 126.6.	29
Figure 16 – Example of AA block source with: SC = 74.3%, DF = 6.4 Hz, and kurtosis = 177.	29
Figure 17 – Box-and-whisker plot showing the rank estimated by CAGL for all patients at different CA steps: initial (before ablation); intermediary (CA between the first and penultimate steps); outcome (after the last CA step). The n indicates the number of ECG segments in each box. .	31
Figure 18 – Box-and-whisker plot at the beginning of CA and after PVI for the group of 17 patients who underwent this CA step.	31
Figure 19 – Scatter plot of the initial estimated rank (before CA) of the block that provides the AA signal and AF recurrence. A negative correlation can be observed.	32

Figure 20 – Computing the condition number (σ) vs. the number of samples (N) to build the matrix using different values of $\Delta\omega$. For each curve, the diamond marker indicates the minimum value of N to have $\text{rank}(\mathbf{H}_s) = 2$.	34
Figure 21 – Number of samples N necessary to build a Hankel matrix \mathbf{H}_s , with $R = L$, versus the distance between poles ($\Delta\omega$). variation.	35
Figure 22 – Number of samples N necessary in the windowed signal $y(n)$ to build \mathbf{H}_s , with $R = L$, versus the SNR values, and fixed distance between poles $\Delta\omega = 0.05$ for 100 Monte Carlo runs.	36
Figure 23 – Further results of experiments from Figure 10 (a), but with different values for τ , as shown on subtitle.	43
Figure 24 – Further results of experiments from Figure 10 (b), but with different values for γ_0 , as shown on subtitle.	43
Figure 25 – Scatter plot describing the rate of true structure estimation for each τ , and each color represents a γ -region.	44

LIST OF TABLES

Table 1 – Unconstrained AGL parameters.	16
Table 2 – Structure estimation accuracy in three Monte Carlo experiments with 500 initialization.	21
Table 3 – Model parameters.	24
Table 4 – Overall population characteristics.	28

CONTENTS

1	INTRODUCTION	1
1.1	Related publications	3
1.2	Work Organization	3
2	ELECTROPHYSIOLOGICAL BACKGROUND	5
2.1	Healthy Heart: Normal Sinus Rhythm	5
2.2	Atrial Fibrillation	7
2.3	Step-wise Catheter Ablation	8
3	COMPLEXITY ANALYSIS	9
3.1	Notation	9
3.2	Blind Source Separation	9
3.3	Low-Rank Hankel Source Model	11
3.4	Block Term Decomposition	13
3.5	Alternating Group Lasso for Block-Term Tensor Decomposition . . .	16
3.6	Vandermonde Matrix and Pole Distance	17
3.7	Singular Value Decomposition	18
4	RESULTS AND DISCUSSION	19
4.1	Synthetic Scenario	19
4.1.1	<i>AGL Setup</i>	19
4.1.2	<i>AGL parameters (γ, τ) tuning</i>	21
4.2	Semi-Synthetic Scenario	23
4.2.1	<i>CAGL</i>	23
4.2.2	<i>AA Model</i>	23
4.2.3	<i>CAGL Setup</i>	26
4.3	Real ECG Scenario	28
4.3.1	<i>Tensor-Based AF Complexity Index</i>	28
4.3.2	<i>Database and Experimental Setup</i>	28
4.3.3	<i>Catheter Ablation impact to Atrial Activity Complexity</i>	30
4.3.4	<i>Atrial Fibrillation Recurrence and Complexity</i>	31
4.4	Hankel Signal Model	33
4.4.1	<i>Condition Number</i>	33
4.4.2	<i>Sample Size for a Full-Rank Hankel Matrix</i>	34
4.4.3	<i>Noisy Scenario and SNR Threshold</i>	35
5	CONCLUSION	37
5.1	Further Work	38
	REFERENCES	39
	APPENDIX A	42
	APPENDIX B	45

1 INTRODUCTION

A healthy heart works as a blood pump to the human body. It contracts and relaxes to a regular beat pattern called sinus rhythm. A small cluster of cells at the atria trigger an electrical signal and it spreads through the heart, then it contracts and forces the blood into the ventricles. After that they contract and pump blood out of the heart as electrical signals reach ventricular muscle cells. Heart-related diseases that affect the regular beat pattern are of major clinical, social and economic concern, impacting in reduction of quality of life, since they are associated with an increased risk of stroke, heart failure, and mortality. Atrial fibrillation (AF) is one of them and can be primarily considered as a supraventricular arrhythmia characterized by chaotic and uncoordinated atrial activation and contraction (MAINARDI et al., 2008), impairing sinus rhythm.

Since AF is the most frequent sustained arrhythmia encountered in clinical practice and is responsible for an increasingly high number of hospitalizations and deaths (JANUARY et al., 2014), this challenging cardiac condition is also known as the last great frontier in cardiac electrophysiology. At least about 4.2 million people suffer from this disease in Europe and the USA (MAINARDI et al., 2008), however the electrophysiological mechanisms responsible for its triggering and maintenance are not completely understood.

The atrial activity (AA) signal analysis from the standard 12-lead electrocardiogram (ECG) is a non-invasive and cost-effective way to study this cardiac rhythm disorder. However, the AA during AF is characterized by low-amplitude fibrillatory waves, called f-waves, that are masked by the QRS complex responsible for the ventricular activity (VA) in each heartbeat. In addition, the AA sometimes presents an amplitude lower than the noise, hampering its analysis.

Since the AA and the VA signals are typically assumed uncoupled during AF, that the extraction of AA from the ECG admits a blind source separation (BSS) formulation (RIETA; CASTELLS; SÁNCHEZ, et al., 2004). The (BSS) is a well-known approach in signal processing, which consists in the estimation of a set of source signals based on the observation of a set of mixed signals, and it usually relies on matrix decompositions. Nevertheless, strong mathematical constraints are necessary to assure uniqueness of the decomposition, such as mutual orthogonality between spatial factors and statistical independence (ZARZOSO, 2009a; ZARZOSO; COMON, 2010).

In order to overcome these limitations, tensor decompositions are powerful tools, ensuring uniqueness and outperforming matrix-based methods under milder constraints (M. R. DE OLIVEIRA; ZARZOSO, 2019). A celebrated tensor-based method is the block term tensor decomposition (BTD) (DE LATHAUWER, 2011; M. GOULART et al., 2020). This technique takes advantage of discrete-time signals that can be modeled as linear combinations of exponentials (all-pole models). Since the sources can be expressed

as low-rank Hankel matrices, the signal separation can be performed via BTD. The Hankel matrix built from such source signals accepts the Vandermonde decomposition (BOLEY et al., 1997), a well-known result in problems of matrix analysis and telecommunications. Different fields in signal processing take advantage on low-rank Hankel source models for speech analysis (WERUAGA; AL-KHAYAT, 2006), black-box polynomial analysis (BECKER-ERMANN et al., 2007), and tensor decompositions (DE LATHAUWER, 2011), some applied to biomedical signal analysis (M. GOULART et al., 2020; ABDALAH et al., 2020). In this scenario, the BTD built from Hankel matrices, proposed as a technique to solve BSS problems in (DE LATHAUWER, 2011), may be used to noninvasively extract the AA signal from AF ECG recordings, showing that it can outperform the matrix-based techniques in this particular application (DE OLIVEIRA; ZARZOSO, 2019; ZARZOSO, 2017).

Several new therapies for AF are studied, from drugs to surgical procedures. Step-wise catheter ablation (CA) is an effective therapy to treat persistent AF and restore sinus rhythm (KIRCHHOF; CALKINS, 2016). Hence, methods to measure AA complexity at each procedural step are relevant to improve clinical analysis and guide CA in real-time. Furthermore, it would be desirable to clarify the impact of each intervention step in AF, as pulmonary vein isolation (PVI) and others widely used techniques (HAÏSSAGUERRE et al., 1998), (SEITZ et al., 2017). However, existing methods for noninvasive quantification of AF complexity require sufficiently long ECG recordings, hindering their use in clinical practice.

Aiming to overcome such limitations, the present work applies the recently proposed algorithm Alternating Group Lasso (AGL) and its constrained version (CAGL) to compute the BTD for solving the BSS problem (M. GOULART et al., 2020). CAGL is able to jointly extract the AA signal from the ECG and measure AF complexity, from very short recordings. AF complexity is measured from the rank of the tensor block correlated with the AA signal (ABDALAH et al., 2020).

1.1 Related publications

During the development of this work, the following scientific contributions have been published (ABDALAH et al., 2020, 2021):

- L. Abdalah, P. M. R. Oliveira, W. Freitas Jr., V. Zarzoso, “Tensor-based noninvasive atrial fibrillation complexity index for catheter ablation”, *Computing in Cardiology*, Rimni, Italy, Sep. 13-16, 2020, accepted for publication and presentation.
- L. Abdalah, W. Freitas Jr., P. M. R. Oliveira, V. Zarzoso, “Low-Rank Hankel Signal Model: Numerical Results”, *Simpósio Brasileiro de Telecomunicações e Processamento de Sinais*, Fortaleza, Brazil, Sep. 27, 2021, accepted for publication and presentation.

1.2 Work Organization

This document is organized into five parts, each comprised of a number of sections.

- I. Chapter 1: Synthesis and introduction to the work;
- II. Chapter 2: Electrophysiological background;
- III. Chapter 3: Complexity analysis method formulation;
- IV. Chapter 4 Computational experiments proposition and its results;
- V. Chapter 5 Discussion, important remarks, conclusion and further work.

Furthermore, the Appendix presents extra results for the parameters tuning scenario, and the conference papers that have been published.

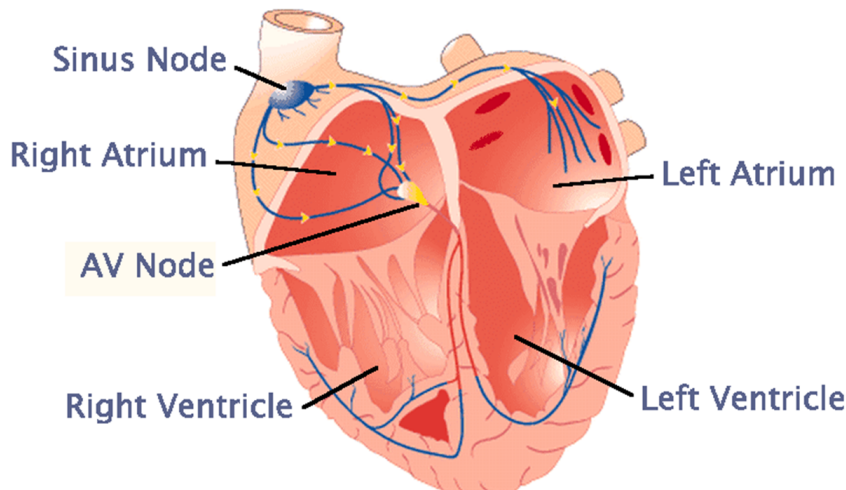
2 ELECTROPHYSIOLOGICAL BACKGROUND

The heart is a crucial organ to our body and how it works has been the subject of study from Ancient times, passing through *de Motu Cordis* (William Harvey) to nowadays. Its functioning mechanisms and diseases have an extensive literature, including studies that try to relate diseases and signal processing techniques as this work.

2.1 Healthy Heart: Normal Sinus Rhythm

The heart works as a pump to the human body, the blood enters the atria while it is relaxed and then moves into the ventricles, these phenomena are called, respectively, diastole and systole. A healthy heart contracts and relaxes to a regular beat pattern called “sinus rhythm”. This pattern starts at the sinoatrial (SA) or sinus node, the “biological pacemaker” (AMBESH; KAPOOR, 2017), where a small cluster of cells triggers an electrical signal that spreads down to the atrioventricular (AV) node. As the atria contract, they force blood into the ventricles. Then the ventricles contract and pump blood out of the heart as electrical signals reach ventricular muscle cells (see Figure 1).

Figure 1 – Heart’s structure.



Source: New Health Guide¹.

A way to study the behavior of the heart is using the standard 12-lead ECG, a noninvasive technique that uses sensors on the patient’s skin to measure the electrical activity from the heart, taking advantage of the spatial diversity. In a conventional 12-lead ECG, the electrodes are placed on the patient’s limbs and on the surface of the chest, 6 each. These electrodes are referred to as leads. A lead is a potential difference obtained from two ECG electrodes and they consist in three bipolar limb leads (I, II, and III), three unipolar limb leads (AVR, AVL, and AVF), and six unipolar chest leads (V1, V2, V3, V4, V5, V6), also called V leads.

¹ Available on <https://www.newhealthguide.org/What-Is-The-Pacemaker-Of-The-Heart>.

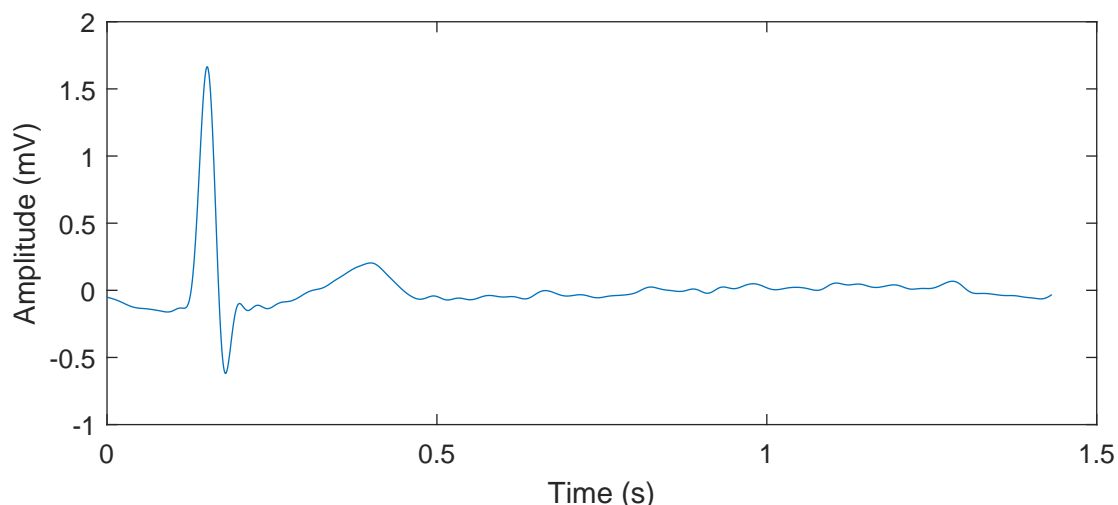
The electrodes record the magnitude measure of the heart's electrical potential over a period of time. Hence, the overall magnitude and direction of the electrical depolarization on the heart is captured at each moment throughout the cardiac cycle. The lead V5 is shown in Figures 2, 3.

Figure 2 – Heartbeat sequence present in Lead V5 from a standard 12-lead ECG, without a frame.



Source: Prepared by the author.

Figure 3 – Single Heartbeat representation in Lead V5 from a standard 12-lead ECG.



Source: Prepared by the author.

2.2 Atrial Fibrillation

AF is a cardiac arrhythmia that affects at least 4.2 million people and is believed to be responsible for a quarter of brain strokes. AF is indeed the most common sustained cardiac arrhythmia encountered in clinical practice (JANUARY et al., 2014).

The pathophysiology, which means the disordered physiological processes associated that leads to AF, are complex and not completely understood. Nevertheless, it results from an uncoordinated spread of electrical impulses throughout out the atria impairs for the regular flow of blood pumping in the heart, may cause clots, heart failure, strokes and may even lead to death. Early experimental studies suggested the presence of an intrinsic organization of AA during AF, whose triggering and maintenance may is due to multiple reentrant wavelets (MAINARDI et al., 2008).

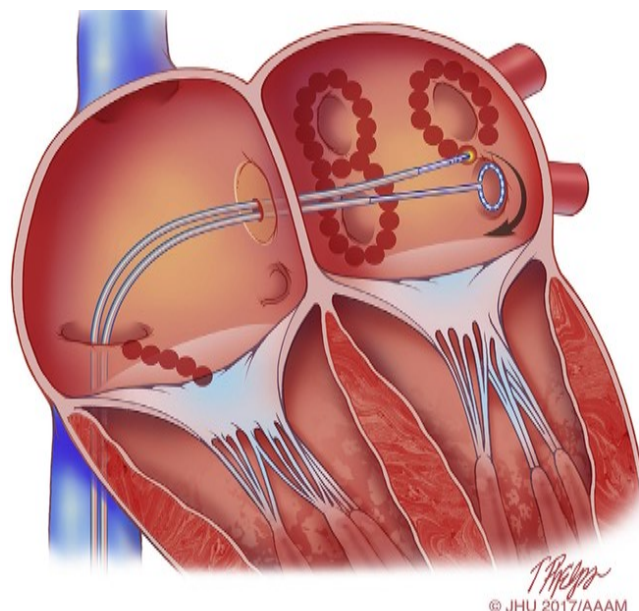
A quivering at the heart is a recurrent way to explain AF symptom. The irregular electrical signals disrupt the normal condition between the sinoatrial and atrioventricular nodes resulting in quivering at the atria, see Figure 1. This prevents them from effectively moving blood into the ventricles. In a ECG it results in the P wave being replaced by fibrillatory waves, called f waves, where f is from fibrillatory. F waves occur throughout the recording, but are masked by the QRST complex of VA at each heartbeat. They can be observed in Figure 3, after 0.5 seconds. In addition, this f waves can be represented as complex exponential sums (all-pole model) (DE LATHAUWER, 2011) and is the core of this study.

This disorder can be studied by invasive direct contact mapping, although there is an increasing interest in noninvasive methodologies. The most appropriate treatment depends on severity, length of the AF and medical issues that the patient might have. It could be medications, nonsurgical and/or surgical procedures. One of them is the subject of the report: Catheter ablation.

2.3 Step-wise Catheter Ablation

Catheter ablation is a surgical procedure, where the cardiologist introduce a catheter in the groin blood vessel. To locate the tissue that is causing your arrhythmia, the doctor can send a small electrical impulse through the electrode catheter or record the heart's electrical signals. Then, radiofrequency energy is delivery from the catheter to scar a small area of heart tissue thought to be responsible for AF triggering and maintenance. This scarring procedure is repeated until the AF is mitigated and/or patient restore sinus rhythm.

Figure 4 – Catheter ablation procedure.



Source: Tim Helps © 2017 Johns Hopkins University, AAM².

Severe steps are typically carried out. The most common procedure is the step-wise catheter ablation (CA), an effective therapy to treat persistent AF. (KIRCHHOF; CALKINS, 2016). After the groundbreaking discovery about pulmonary veins (PV) role in AF inducing and maintenance (HAÏSSAGUERRE et al., 1998), pulmonary veins isolation (PVI) become an relevant technique on the step-wise CA. Other techniques are widely used and subject of study (SEITZ et al., 2017), for example, fragmented potentials. The procedure choice depend on the patient specificities, although CA is frequently indicate to patients with AF due to its good success rate.

²Available on https://www.researchgate.net/publication/319871328_2017.

3 COMPLEXITY ANALYSIS

The AF complexity can be used as an index to support clinical decisions and guide real time CA. However, existing methods for noninvasive quantification of AF complexity are limited due to the fact that sufficiently long ECG recordings are required and they have limited , hindering their use in clinical practice.

A BSS approach can be applied aiming isolate signal sources responsible for atrial activation, and usually rely on matrix decompositions. Nevertheless, strong mathematical constraints are necessary assure uniqueness of the decomposition, such as mutual orthogonality between spatial factors and statistical independence. The most-known matrices methods are based on entropy, spectral density, principal and independent (RIETA; CASTELLS; SÁNCHEZ, et al., 2004), (ZARZOSO, 2009b), (MARINHO R. DE OLIVEIRA; ZARZOSO, 2018).

In order to overcome this limitations, the ECG data can be arranged using a tensorial approach, to explore milder constraints to its assure its uniqueness and out-perform matrix-based methods estimation quality (DE OLIVEIRA; ZARZOSO, 2019), (ZARZOSO, 2017), (RIBEIRO et al., 2015).

3.1 Notation

Scalars, vectors, matrices and tensors are represented by lower-case (a, b, \dots), boldface lower-case ($\mathbf{a}, \mathbf{B}, \dots$), boldface capital ($\mathbf{A}, \mathbf{B}, \dots$) and calligraphic ($\mathcal{A}, \mathcal{B}, \dots$) letters, respectively.

The symbol \circ represents the outer (tensor) product, $|\cdot|$ represents the absolute value, matrix transpose is represented by $(\cdot)^\top$, symbol $\|\cdot\|$ represents the ℓ_2 -norm. The operator $\text{Diag}(\cdot)$ builds a diagonal matrix by placing its arguments along the diagonal, and a hat ($\hat{\cdot}$) denotes an estimate.

The notations $\|\cdot\|_F$ and $\|\cdot\|_{2,1}$ stand for the Frobenius norm and the matrix mixed $\ell_{2,1}$ -norm, respectively.

3.2 Blind Source Separation

The estimation of AA during AF ECG's accepts a BSS model, as described in (CASTELLS et al., 2005), (RIETA; CASTELLS; SÁNCHEZ, et al., 2004).

This Section formulation is based on (RIBEIRO et al., 2015), (CARDOSO, 1998).

The simplest model of blind source separation (BSS) assumes the existence of independent unobserved and observed data, respectively, $\mathbf{S} \in \mathbb{R}^{K \times N}$ and $\mathbf{Y} \in \mathbb{R}^{K \times N}$, where K represent leads/channels and N the number of samples.

The observed data is considered being linear and instantaneous mixtures, i.e, each $\mathbf{y}_i(n)$ lead in \mathbf{Y} for , comes from:

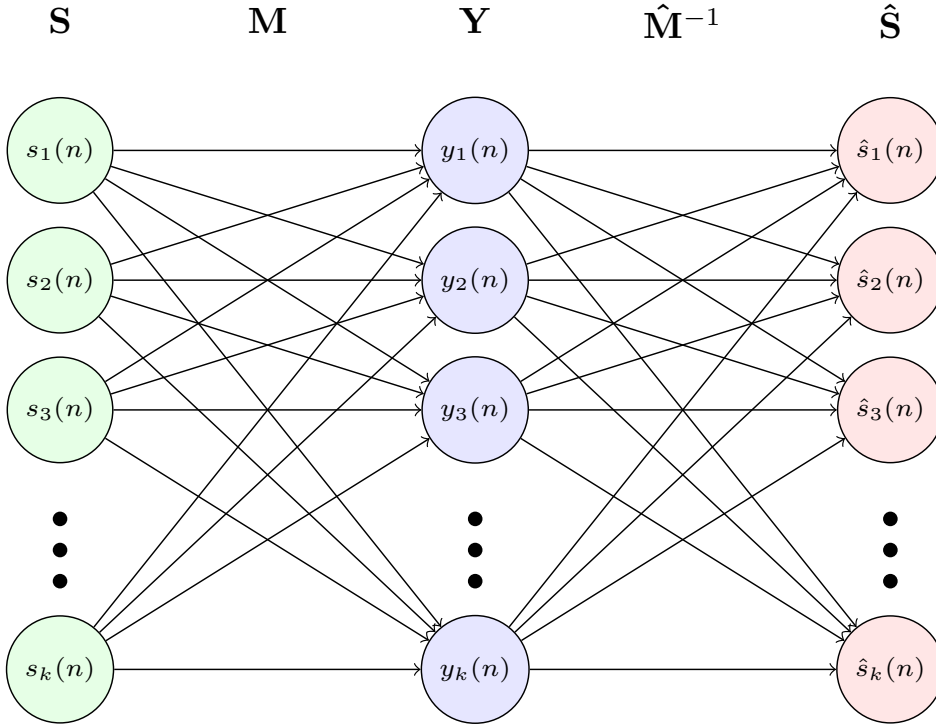
$$\mathbf{y}_i(n) = \sum_{k=1}^K m_{ik} \mathbf{s}_k(n), \quad i = 1, \dots, K, \quad (1)$$

A compact representation is the matrix formulation for the mixing equation in (2).

$$\mathbf{Y} = \mathbf{MS}. \quad (2)$$

When observing multiple ECG leads, the AA extraction problem can be modeled from the perspective of BSS, where \mathbf{M} is the mixing matrix representing the travel path of the electrical signal, from the heart through the body until reach each ECG sensor.

Figure 5 – Node diagram of a simple BSS model.



Source: Prepared by the author.

The diagram in Figure 5 illustrates the BSS problem, where: nodes in green, blue and red represent source, observed signal and estimated sources, respectively. While, each line stands for the coefficient which weights each node. The left part of the diagram (\mathbf{S} and \mathbf{M}) is unknown in real problems. The middle (\mathbf{Y}) is the only prior information. The right part ($\hat{\mathbf{S}}$ and $\hat{\mathbf{M}}$) is estimated using different matrix-based techniques as principal component analysis (PCA) and independent component analysis (ICA).

Another advantage of visualizing the problem as a diagram is an interesting interpretation. Because the lines below \mathbf{M} represents the collection of all weights m_{ik} in equation (1). Since all weights are unknown, is necessary to estimate $\hat{\mathbf{M}}^{-1}$, the mixing matrix inverse, to find the estimated sources $\hat{\mathbf{S}}$.

3.3 Low-Rank Hankel Source Model

Assume that if a discrete time signal $s(n)$ is a linear combination of L damped complex exponentials, say:

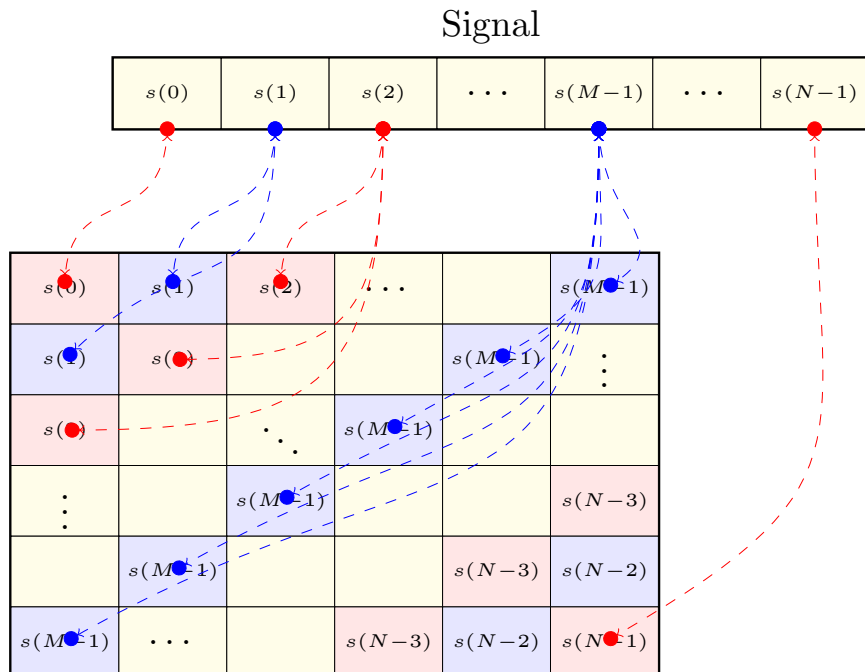
$$s(n) = \sum_{l=1}^L c_l z_l^n, \quad 0 \leq n \leq N-1 \quad (3)$$

where $c_l, z_l \in \mathbb{C}$, are coefficients and poles, respectively.

The sequence $s(n)$ can be mapped onto an $(M \times M)$ Hankel matrix denoted \mathbf{H}_s , where each sample is placed along the anti-diagonal of \mathbf{H}_s as shown in Fig. 6, with mapping function $\mathbf{H}_{s(i,j)} = s(i+j-1)$, for i th row, and j th column. We assume N is odd without loss of generality, hence:

$$M = \frac{N+1}{2}. \quad (4)$$

Figure 6 – Visual representation of a Hankel matrix \mathbf{H}_s built from a signal $s(n)$.



Source: Prepared by the author.

A major result in signal processing states that \mathbf{H}_s accepts the following Vandermonde decomposition (BOLEY et al., 1997; DE LATHAUWER, 2011):

$$\mathbf{H}_s = \mathbf{V}_s \mathbf{D} \mathbf{V}_s^\top \quad (5)$$

where \mathbf{V}_s is the Vandermonde matrix

$$\mathbf{V}_s = \begin{bmatrix} 1 & 1 & \dots & 1 \\ z_1 & z_2 & \dots & z_L \\ \vdots & \vdots & & \vdots \\ z_1^{M-1} & z_2^{M-1} & \dots & z_L^{M-1} \end{bmatrix} \in \mathbb{C}^{M \times L}, \quad (6)$$

and $\mathbf{D} = \text{diag}(c_1, c_1, \dots, c_L) \in \mathbb{C}^{L \times L}$ is a diagonal matrix.

As result of the Vandermonde decomposition (6), matrix \mathbf{H}_s has rank at most $\min\{L, M\}$. Hence, a first remark is that the more poles a given signal is composed of, the higher the rank of its Hankel matrix. This observation underlies the use of $\text{rank}(\mathbf{H}_s)$ as a measure of signal complexity. Nevertheless, a Hankel matrix build from a signal $s(n)$ with L poles needs to map at least N_{min} samples:

$$N_{min} = 2L - 1, \quad (7)$$

to present its rank R equal to L (DE LATHAUWER, 2011; BOLEY et al., 1997; M. GOULART et al., 2020). As soon as this minimum threshold is observed, the rank R should be equal to the number of poles L for a signal following model (3), regardless of the sample size.

3.4 Block Term Decomposition

Relying on the low-rank Hankel source model, the signal separation can be performed by via Block Term Decomposition (BTD).

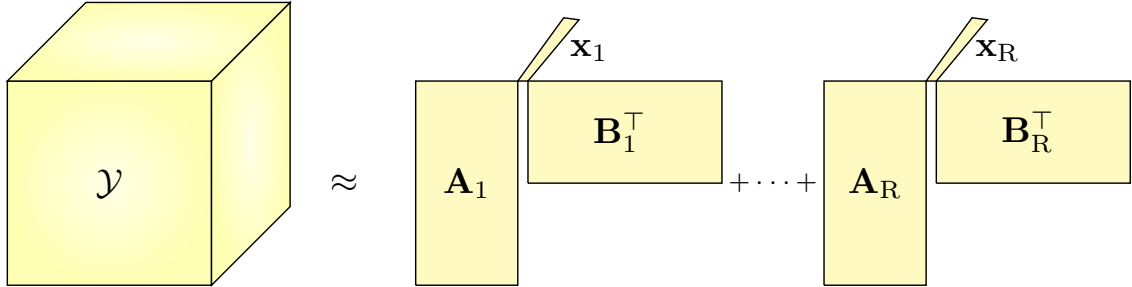
Firstly, we can think of a tensor as a collection of matrix, stacking on a third dimension. So given an arbitrary third-order tensor $\mathcal{Y} \in \mathbb{R}^{I \times J \times K}$ its BTD is written as:

$$\mathcal{Y} = \sum_{r=1}^R \mathbf{H}_r \circ \mathbf{x}_r \quad (8)$$

where R is the number of blocks, $\mathbf{x}_r \in \mathbb{R}^K$ is nonzero and $\mathbf{H}_r \in \mathbb{R}^{I \times J}$ is a structured matrix that has rank L_r , admitting the factorization $\mathbf{H}_r = \mathbf{A}_r \mathbf{B}_r^\top$, where $\mathbf{A}_r \in \mathbb{R}^{I \times L_r}$ and $\mathbf{B}_r \in \mathbb{R}^{J \times L_r}$ have rank L_r . We may then rewrite (8) as:

$$\mathcal{Y} = \sum_{r=1}^R (\mathbf{A}_r \mathbf{B}_r^\top) \circ \mathbf{x}_r \quad (9)$$

Figure 7 – The block term decomposition $(L_r, L_r, 1)$ representation of an arbitrary third-order tensor.



Source: Prepared by the author.

To take advantage on BTD model, that is shown in Figure 7, consider a linear instantaneous mixture

$$y(n) = \sum_{r=1}^R x_r s_r(n), \quad (10)$$

with $s_r(n)$ following the proposed model (3), for each value of r , and $L < M$.

Consider that one wants to estimate the signals $s_r(n)$ from knowledge of y (and of the previous model) only. By linearity of the Hankel map, we have $y \mapsto \mathbf{H}_y$, where

$$\mathbf{H}_y = \sum_{l=1}^R x_l \mathbf{H}_{s_l} \quad (11)$$

so that $\text{rank } \mathbf{H}_y \leq \sum_{r=1}^R L_r$ (M. GOULART et al., 2020). Though, this linear combination of matrices is not of much help for separation, without further information.

The scenario changes with the introduction of spatial diversity, meaning we now observe $y(k, n) = \sum_{r=1}^R x_{k,r} s_r(n)$ for $k = 1, \dots, K$. In matrix notation, we have

$$\mathbf{Y} = \mathbf{X}\mathbf{S}^\top \quad (12)$$

where $\mathbf{S} = s_r(n) = s_r(n - 1)$ is an $N \times R$ matrix containing the source signals and $\mathbf{X} = (x_{k,r})$ is a $K \times R$ mixture matrix specifying how the sources are combined to yield the channels' outputs, as the equation (2). Each such output $y_k(n) = y(k, n)$ for a fixed k , according to each row of \mathbf{Y} , can be mapped into an $M \times M$ Hankel matrix as before, as discussed in Section 3.3 and shown in Figure 6.

Hence, $\mathbf{Y}_k = \sum_{r=1}^R x_{k,r} \mathbf{H}_r$, where \mathbf{H}_r is the rank- L_r Hankel matrix associated with s_r . The matrices \mathbf{Y}_k can be viewed, as shown in Figure 8, as frontal slices. *i.e*, stacking matrices on its third dimension. of an $M \times M \times K$ tensor \mathcal{Y}_k satisfying (13).

$$\begin{aligned} \mathcal{Y} &= \sum_{k=1}^K \mathbf{Y}_k \circ \mathbf{e}_k = \sum_{k=1}^K \left(\sum_{r=1}^R x_{k,r} \mathbf{H}_r \right) \circ \mathbf{e}_k \\ &= \sum_{r=1}^R \mathbf{H}_r \circ \left(\sum_{k=1}^K x_{k,r} \mathbf{e}_k \right) \\ &= \sum_{r=1}^R \mathbf{H}_r \circ \mathbf{x}_r \end{aligned} \quad (13)$$

where \mathbf{e}_k is the k th canonical basis vector of \mathbb{C}^K and \mathbf{x}_r is the r th column of \mathbf{X} .

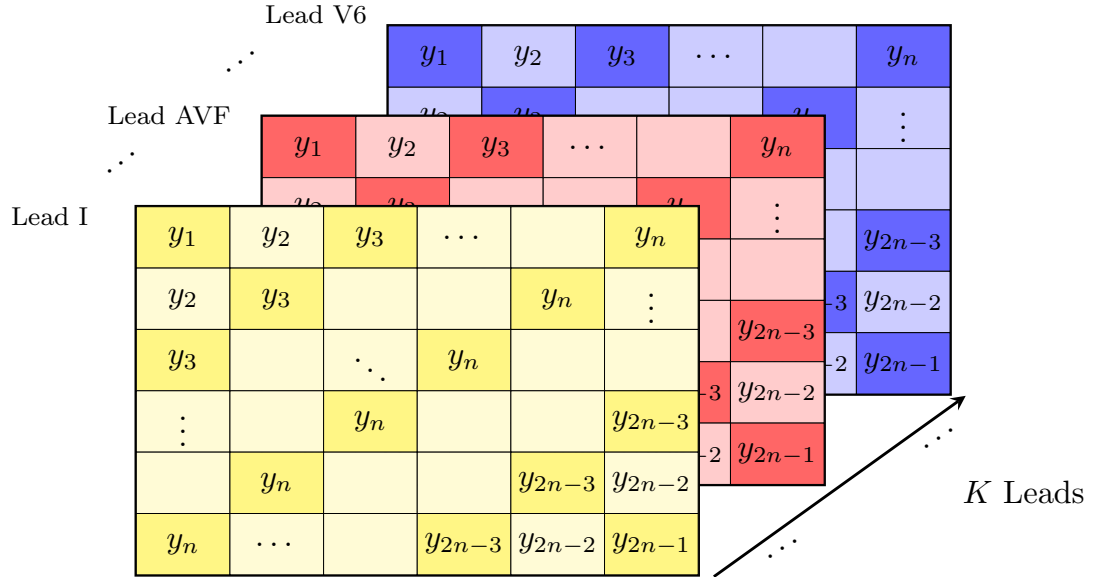
Following the framework proposed previously, an ECG recording \mathbf{Y} from K leads composed by N time samples can be modeled as a matrix factorization in equation (2), where $\mathbf{M} \in \mathbb{R}^{K \times R}$ is the mixing matrix, modeling the propagation of the cardiac electrical sources from the heart to the body surface, $\mathbf{S} \in \mathbb{R}^{R \times N}$ is the source matrix that contains mainly the atrial and ventricular sources and R is the number of sources (RIETA; CASTELLS; SÁNCHEZ, et al., 2004). Furthermore, \mathbf{Y} can be mapped in a third-order tensor \mathcal{Y} (Figure 8) that admits a BTD model, written as:

$$\mathcal{Y} = \sum_{r=1}^R \mathbf{H}_{\mathbf{S}}^{(r)} \circ \mathbf{m}_{\cdot r} \quad (14)$$

where $\mathbf{H}_{\mathbf{S}}^{(r)}$ is a Hankel matrix built from the r^{th} source of \mathbf{S} . The Hankel-BTD suits the characteristics of AA in AF episodes, since atrial signals can be approximated by a sum of complex exponentials and mapped onto Hankel matrices with rank equal to the number of

poles (ZARZOSO, 2017). Indeed, due to the quasi-periodic nature of AF signals, atrial sources can be well-modeled by a sum of exponentials (STRIDH; SÖRNMO, 2001).

Figure 8 – Tensor representation: each lead mapped into a Hankel matrix and stacked on its third mode.



Source: Prepared by the author.

3.5 Alternating Group Lasso for Block-Term Tensor Decomposition

In general, an approximate BTD is computed by minimizing the Euclidean distance between the observed data tensor $\mathcal{Y} \in \mathbb{X}^{I \times J \times K}$ and a model of fixed structure with respect to the model components:

$$f(\mathbf{A}, \mathbf{B}, \mathbf{X}) \triangleq \left\| \mathcal{Y} - \sum_{r=1}^R (\mathbf{A}_r \mathbf{B}_r^\top) \circ \mathbf{x}_r \right\|_F^2 \quad (15)$$

Still, algorithms based exclusively on (15) are strongly dependent on the initialization of its matrix factors and do not estimate the model parameters, i.e., the number of blocks and their ranks.

To overcome such limitations, instead of using a fixed BTD structure as (15), an algorithm called AGL and its constrained version described for Hankel matrices called CAGL, are proposed in (M. GOULART et al., 2020). This method includes penalization terms promoting low-rank blocks and controlling the number of blocks as:

$$F(\mathbf{A}, \mathbf{B}, \mathbf{X}) \triangleq f(\mathbf{A}, \mathbf{B}, \mathbf{X}) + \gamma g(\mathbf{A}, \mathbf{B}, \mathbf{X}) \quad (16)$$

where $\gamma > 0$ is a regularization parameter and g is a regularization function of the form:

$$g(\mathbf{A}, \mathbf{B}, \mathbf{X}) \triangleq \|\mathbf{A}\|_{2,1} + \|\mathbf{B}\|_{2,1} + \|\mathbf{X}\|_{2,1} \quad (17)$$

Due to the geometric properties of the mixed $\ell_{2,1}$ -norm, solutions where \mathbf{A} , \mathbf{B} and \mathbf{X} have null columns (for sufficiently high γ values) will be induced, allowing one to select the relevant low-rank blocks. This method is called group lasso and is a generalization of the the lasso estimator principle (YUAN; LIN, 2006).

In order to enforce a unique solution to this problem, a proximal term τ is added to the standard group lasso problem, as described in (M. GOULART et al., 2020).

Table 1 – Unconstrained AGL parameters.

Parameters	
Input	\mathcal{Y} R L γ τ $\mathbf{A}^{(0)} \mathbf{B}^{(0)} \mathbf{X}^{(0)}$
Output	$\hat{\mathbf{A}}$ $\hat{\mathbf{B}}$ $\hat{\mathbf{X}}$

Source: Prepared by the author.

The input parameters represent, respectively, Data tensor, number of blocks, guess of the block rank, penalty parameters, proximal term weight and the initial factor matrices, whereas the output parameters are the estimated factor matrices.

3.6 Vandermonde Matrix and Pole Distance

When a signal is a sum of complex exponentials (3), its poles are closely linked to the columns of matrix \mathbf{V}_s , according to equation (6). If the distance between these poles decreases, the columns of \mathbf{V}_s become closer to each other, having an impact on the Hankel matrix rank. Consequently, an investigation about the relationship between a signal mapping and its matrix rank deficiency may be proposed to ensure that the separation estimate the rank equal to number of damped complex exponential.

To illustrate this behavior, we assume two poles $z_1 = e^{j\omega_1}$ and $z_2 = e^{j\omega_2}$, and the corresponding Vandermonde vectors $\mathbf{v}_1 = [1, e^{j\omega_1}, e^{j2\omega_1}, \dots, e^{j(M-1)\omega_1}]^\top$ and $\mathbf{v}_2 = [1, e^{j\omega_2}, e^{j2\omega_2}, \dots, e^{j(M-1)\omega_2}]^\top$. We can observe that each vector norm is equal to M , and the columns scalar product leads to equation (18).

$$\begin{aligned} \|\mathbf{v}_1\| &= \|\mathbf{v}_2\| = M, \\ \mathbf{v}_1^\top \mathbf{v}_2 &= \sum_{n=0}^{M-1} e^{-jn\omega_1} e^{jn\omega_2}. \end{aligned} \quad (18)$$

Finally, replacing $\Delta\omega = (\omega_2 - \omega_1)$ and the exponential identities we have that the scalar product becomes:

$$\cos(\theta) = \frac{\mathbf{v}_1 \cdot \mathbf{v}_2}{\|\mathbf{v}_1\| \|\mathbf{v}_2\|} = \frac{\sin(M \frac{\Delta\omega}{2})}{M \sin(\frac{\Delta\omega}{2})}. \quad (19)$$

Based on the previous result, we can ensure that when $\Delta\omega$ tends to zero for a fixed M , we have the equation (20), showing that the columns becomes colinear, as expected, if the distance between poles ($\Delta\omega$) become too small. In this case, if we compare the singular values, the Hankel matrix rank is equal to one. This shows mathematically that a minimum distance between poles is required in practical scenarios. In this case, the equivalent Hankel matrix rank (R) is equal to one, built from two damped exponentials, resulting in $R \neq L$.

$$\lim_{\Delta\omega \rightarrow 0} \cos(\theta) = 1 \quad (20)$$

However, it is relevant to notice the presence of M in the denominator of equation (19). We can deduce that increasing the value of M used to build \mathbf{V}_s may compensate for the poles proximity. If we replace M using equation (4), we have that:

$$\cos(\theta) = \frac{2 \sin((N+1)\Delta\omega)}{(N+1) \sin(\frac{\Delta\omega}{2})}. \quad (21)$$

Therefore, for a small yet nonzero value of $\Delta\omega$, if we increase N then the scalar-product gets closer to zero (due to N in the numerator), in such a way that colinearity between \mathbf{v}_1 and \mathbf{v}_2 is reduced to equation (22), resulting in $R = L$, in agreement with the classical result observed in the literature (BOLEY et al., 1997).

$$\lim_{N \rightarrow \infty} \frac{2 \sin((N+1)\Delta\omega)}{(N+1) \sin\left(\frac{\Delta\omega}{2}\right)} = 0 \quad (22)$$

3.7 Singular Value Decomposition

The SVD is a valuable tool in signal processing, a common technique for multivariate data analysis and provides a foundation for many other techniques such as principal component analysis (PCA) (WALL et al., 2003).

The SVD of $\mathbf{X} \in \mathbb{C}^{I \times J}$ is given by:

$$\mathbf{X} = \mathbf{U}\Sigma\mathbf{V}^H, \quad (23)$$

where $\mathbf{U} \in \mathbb{C}^{I \times I}$ and $\mathbf{V} \in \mathbb{C}^{J \times J}$ are unitary matrices with orthonormal columns, and the symbol $(\cdot)^H$ denotes the Hermitian operator. Diagonal matrix $\Sigma \in \mathbb{R}^{I \times J}$ contains real, non-negative entries. It can also be represented as $\Sigma = \text{diag}(\lambda_1, \lambda_2, \dots, \lambda_J)$, where each λ_j is a singular value, presented in decreasing order.

In order to compute the rank of \mathbf{X} , a reliable SVD-based method may be applied (GOLUB; LOAN, 2013; BRUNTON; KUTZ, 2019). It consists in performing SVD(\mathbf{X}), then taking the number of singular values $(\lambda_1, \dots, \lambda_J)$ that are larger than a tolerance $\varepsilon = \max(I, J)\mathcal{E}\|\mathbf{X}\|_F$, where \mathcal{E} is the minimum distance that the floating point arithmetic can recognize between two numbers.

Another possible way to assess the source matrix is observing its rank-deficiency by the condition number (σ), taking advantage of the relationship between singular values. The criterion used in this work is the equation 24 that provides a quotient between its maximum and minimum singular values, respectively. A large condition number is linked to a matrix close to rank-deficiency.

$$\sigma = \frac{\lambda_{max}}{\lambda_{min}} \quad (24)$$

4 RESULTS AND DISCUSSION

4.1 Synthetic Scenario

In order to tune the algorithm and assess AGL's estimation accuracy and robustness to initialization, one can apply it to a scenario where the ground-truth is well known.

The performance criterion used to evaluate its accuracy are Normalized Mean Square Error (NMSE) over estimated blocks, written as

$$\text{NMSE}(\hat{\mathbf{A}}, \hat{\mathbf{B}}, \hat{\mathbf{X}}) \triangleq \frac{1}{R} \sum_{r=1}^R \frac{\|(\mathbf{A}_r \mathbf{B}_r^\top) \circ \mathbf{x}_r - (\hat{\mathbf{A}}_r \hat{\mathbf{B}}_r^\top) \circ \hat{\mathbf{x}}_r\|_F^2}{\|(\mathbf{A}_r \mathbf{B}_r^\top) \circ \mathbf{x}_r\|_F^2} \quad (25)$$

and the rate of good structure estimation, the percentage of experiments where the estimated blocks have exactly the original dimensions.

4.1.1 AGL Setup

To assess the estimation, 500 joint realizations of $(\mathbf{A}, \mathbf{B}, \mathbf{X}, \mathcal{N})$ by drawing the (real-valued) elements of \mathbf{A} , \mathbf{B} , \mathbf{X} and \mathcal{N} in an independent and identically distributed (i.i.d.) from the standard normal distribution. \mathbf{X} is then normalized column-wise and the condition $\max_{i,j} |x_i^\top x_j| < 0.9$ is imposed (\mathbf{X} is drawn multiple times until it is met). This prevents nearly collinear spatial signatures.

Next, a noisy model:

$$\mathcal{Y} = \mathcal{Y}_0 + \sigma_{\mathcal{N}} \mathcal{N} \quad (26)$$

is drawn, where $\mathcal{Y}_0 = \sum_{r=1}^R (\mathbf{A}_r \mathbf{B}_r^\top) \circ \mathbf{X}_r$ and $\sigma_{\mathcal{N}}$ is the noise standard deviation, adjusted to obtain a signal-to-noise ratio (SNR) of 20 dB, defined as:

$$\text{SNR} \triangleq \|\mathcal{Y}_0\|_F^2 \sigma_{\mathcal{N}}^{-2} \|\mathcal{N}\|_F^{-2} \quad (27)$$

We set $I = J = 18$, $K = 4$ and $R = 3$. The block ranks are $(L_1, L_2, L_3) = (6, 5, 4)$. Since $L_1 + L_2 + L_3 = 15 < 18 = \min\{I, J\}$, one can compute an approximate initial solution by using an algebraic method implemented by Tensorlab¹.

Given an input tensor and the chosen block ranks \hat{L}_r , this implementation first essentially computes a canonical polyadic decomposition () with rank $\sum_{r=1}^R \hat{L}_r$ and then attempts to cluster the columns of the third factor \mathbf{X} by using a k -means algorithm,

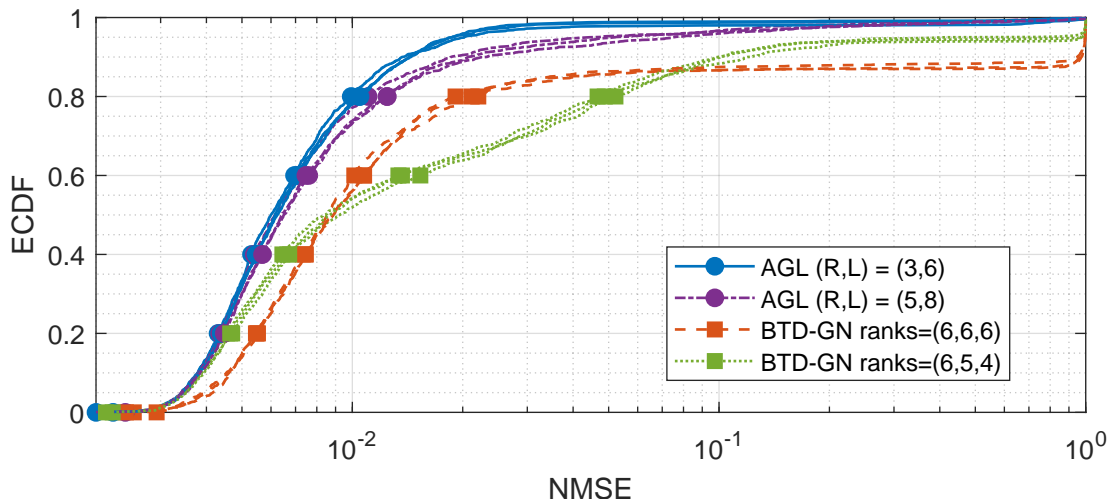
¹The algebraic method is implemented in Tensorlab by the function `ll1_gevd`.

aiming form blocks having the specified ranks. For each realization, AGL is applied with $(R, L) = (3, 6)$, and also with $(R, L) = (5, 8)$, in both cases following these steps:

- An initial solution is generated by applying the described algebraic method with ranks estimates $\hat{L}_1 = \hat{L}_2 = \hat{L}_3 = L$;
- AGL is run from this initial solution using an γ -sweeping procedure with P equispaced values of γ , from a γ_0 to a γ_{P-1} , keeping the last solution. This is inspired by solution-path techniques used in statistics community.

The values used on the γ -sweeping, refered as γ -region, was tuned empirically to the range $[2.5 \times 10^{-1}, 2.5 \times 10^0]$, with $P = 19$. In addition, to compute the NMSE in equation (25), one needs to match the estimated blocks to the ground truth, hence to find the closest estimation, all structure permutation are computed.

Figure 9 – Trend over Empirical CDF's of NMSE over estimated blocks attained by AGL and BTD-GN for 500 realizations of a noise random BTD model (SNR = 20dB).



Source: Prepared by the author.

All this procedure is perfomed three times and the empirical cumulative distribution function (ECDF) of the measured NMSE for each algorithm is shown in Figure 9.

It shows a clear superiority of the proposed approach: for instance, the NMSE attained by AGL is smaller than 0.01 for about 80% realizations with $(R, L) = (3, 6)$ and about 76% realizations with $(R, L) = (5, 8)$ while the same is true for only about 58% in the BTD-GN. Futhermore, the mean rate of good structure estimation (non-inversion on the BTD-GN case) on the same order is: 97.9%, 79.9% and 48.3%. The Table 2 shows the values for each performance.

Table 2 – Structure estimation accuracy in three Monte Carlo experiments with 500 initialization.

Experiment	AGL (3,6)	AGL (5,8)	BTD-GN (6,5,4)
1	98.0%	83.0%	47.8%
2	97.0%	77.2%	48.8%
3	98.6%	79.6%	48.2%

Source: Prepared by the author.

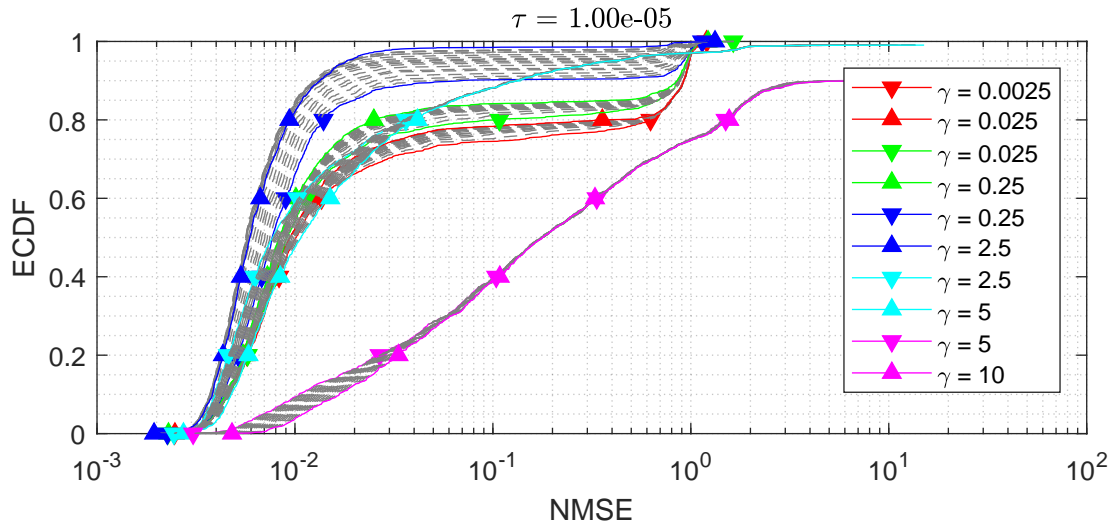
4.1.2 AGL parameters (γ, τ) tuning

Aiming to find an optimal γ -region and τ , the experiment using AGL(3,6) is reproduced using various set of this input parameters. To assess the sensitivity due to γ -region, a value for τ is fixed, while the experiment is performed with $P = 19$, modifying the γ_0 and γ_P . To evaluate τ influence, a γ -region is fixed, and different values of τ are tested. The Figure 23 shows the relationship and robustness over these values.

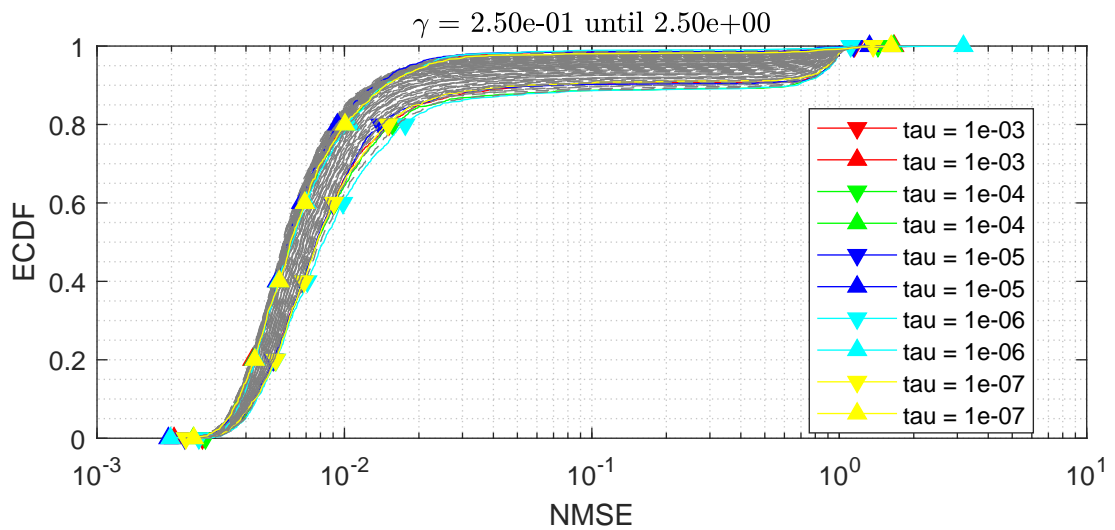
One can assume from the plots that the estimation with $\gamma_0 = 0.25$ has lowest NMSE values. Whereas for different values of τ the trend is not clear. Further results for these experiments reenforcing these statements are available in the Appendix.

Figure 10 – The ECDF of NMSE in the case AGL(3,6), varying both the region used on the γ -sweeping procedure and the proximal term τ . The lower triangles indicate γ_0 's ECDF, while the upper triangles represent the last iteration. The gray curves are intermediaries iterations.

(a) The $\tau = 10^{-5}$ is fixed, and the γ -region is varying in according to the Figure legend.



(b) The γ -region is fixed, range from $\gamma_0 = 0.25$ to 2.5 and τ varying in according to the Figure legend.



Source: Prepared by the author.

4.2 Semi-Synthetic Scenario

In order to assess the BSS with signals similar to ECG recordings, a singal from VA is obtained from the lead V1 of a real ECG, while a signal representing the AA is generated via a model that mimics it proposed in (STRIDH; SÖRNMO, 2001), with some known parameter. This mixture of real and synthetic signals motivate the Section's name.

The ECG matrix \mathbf{Y} is constructed as

$$\mathbf{Y} = \mathbf{V} + \alpha \mathbf{x} \mathbf{s}^\top + \mathbf{N} \in \mathbb{R}^{12 \times N} \quad (28)$$

where \mathbf{V} holds the normalized VA signal, \mathbf{s} holds the AA signal samples, \mathbf{x} is a random spatial signature generated for this source, having standard normal i.i.d., \mathbf{N} contains AWGN samples and α is a scaling factor chosen to obtain an average atrial-to-ventricular power ratio consistent with clinical observations.

Since, we assume that an ECG signal can be represented as a sum of exponentials, as indicated in equation (3), the constrained version of AGL, based on structured Hankel matrices, is exploited.

4.2.1 CAGL

The Constrained Alternating Group Lasso (CAGL) is a special case for this algorithm application. It uses the advantage of a case of interest a signal structured in Hankel matrix. Hence, the estimation must ensure the Hankel structure of the matrix factors at each iteration of AGL, yielding CAGL. So \mathbf{H}_r must belong to the subspace of Hankel matrices with dimensions $(I \times J)$, denoted \mathcal{S}_H , satisfying equation (13). The mode-3 slices $\mathbf{Y}_{..k}$ of the observed tensor are Hankel by construction. However, a solution $(\hat{\mathbf{A}}, \hat{\mathbf{B}}, \hat{\mathbf{X}})$ of (15) may not satisfy $\hat{\mathbf{A}}_r \hat{\mathbf{B}}_r^\top \in \mathcal{S}_H$, due to noise and modeling imperfections. Then, to ensure the Hankel structure at the end of an iterations, a structured low-rank approximation is applied at each iteration, applying the Cadzow's Algorithm (CADZOW, 1988), which consists in performing alternating projections onto the Hankel subspace \mathcal{S}_H , so that $\hat{\mathbf{H}}_r \approx \hat{\mathbf{A}}_r \hat{\mathbf{B}}_r^T \in \mathcal{S}_H$. The work proposed in (M. GOULART et al., 2020) provide further explanation of both AGL and CAGL.

4.2.2 AA Model

This model that mimics AA is given by:

$$\mathbf{s}(n) = - \sum_{p=1}^P a_p(n) \sin(p \theta(n)) \quad (29)$$

with modulated amplitude and phase respectively given by

$$a_p(n) = \frac{2}{p\pi} \left[a + \Delta a \sin \left(2\pi \frac{f_a}{F_s} n \right) \right], \quad (30)$$

and

$$\theta(n) = 2\pi \frac{f_0}{F_s} n + \left(\frac{\Delta f}{F_f} \right) \sin \left(2\pi \frac{F_f}{F_s} n \right). \quad (31)$$

In (STRIDH; SÖRNMO, 2001) two set of parameters are proposed, one of them is chosen at random to build our model, shown in Table 3.

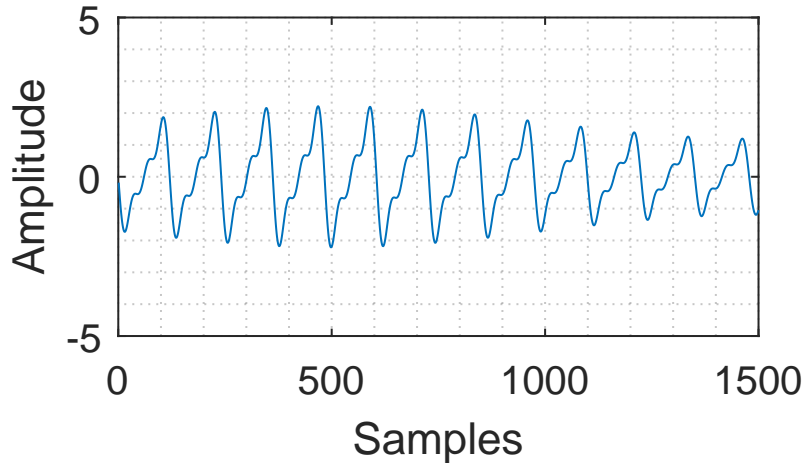
Table 3 – Model parameters.

Experiment	P	a	Δa	f_a	F_s	f_0	Δf	F_f
1	5	150	50	0.08	1000	6	0.3	0.1

Source: Prepared by the author.

The signal generated using this paramets, that mimics AA, is shown in Figure 11.

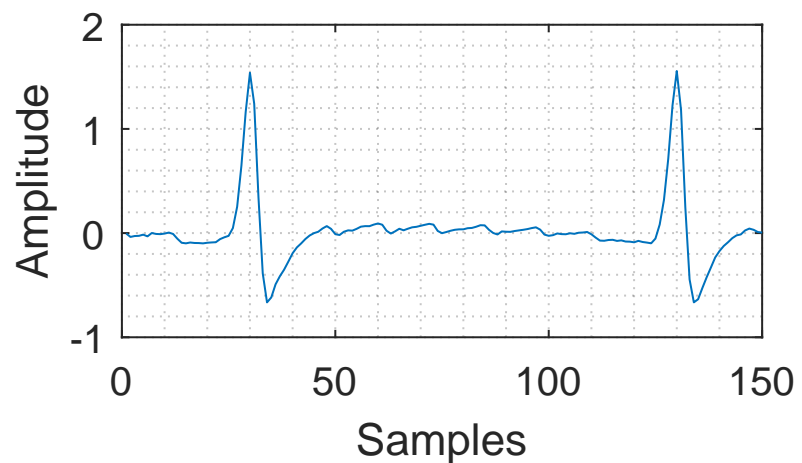
Figure 11 – Signal that mimics AA.



Source: Prepared by the author.

One lead from the semi-synthetic ECG after downsampling is presented in Figure 12, showing clearly the signals of VA and the one that mimics f-waves, responsible for AF.

Figure 12 – Semi-synthetic signal for lead V1 from equation (28) model after downsampling.



Source: Prepared by the author.

4.2.3 CAGL Setup

The synthetic scenario is constructed with small dimensions, hence its computation time is short. However, scenarios for meaningful signals must have way more samples, increasing the computing cost. Aiming to decrease this cost, with practically negligible information loss, we downsample all signals by a factor of 10, since the Nyquist–Shannon sampling theorem is respected. The bandwidth for the lead V1 is shown in Figure 14.

For example a window with yields 1000 samples, a direct Hankelization of this matrix results in a tensor of dimensions $500 \times 501 \times 12$, whose approximate BTD demands a large computing time. The resulting tensor \mathcal{Y} after downsampling have dimensions $50 \times 50 \times 12$.

CAGL is applied to the semi-synthetic recordings with the γ -sweeping procedure, with $P = 50$, the interval $[8 \times 10^{-4}, 0.33 \times 10^{-2}]$, $\tau = 10^{-6}$ and keeping the last solution.

We start the algorithm with the initial guess of $R = 6$ and $L = 40$, i.e, more blocks than sources (2) as in the experiments presented in (M. GOULART et al., 2020), to assess the overestimation.

In general, the estimation for the first values of γ_0 have a number of blocks really close to the initial guess R . However, as the algorithm minimizes the error and tries to match the structure, it gets closer to the original structure, even if the algorithm has no information about it.

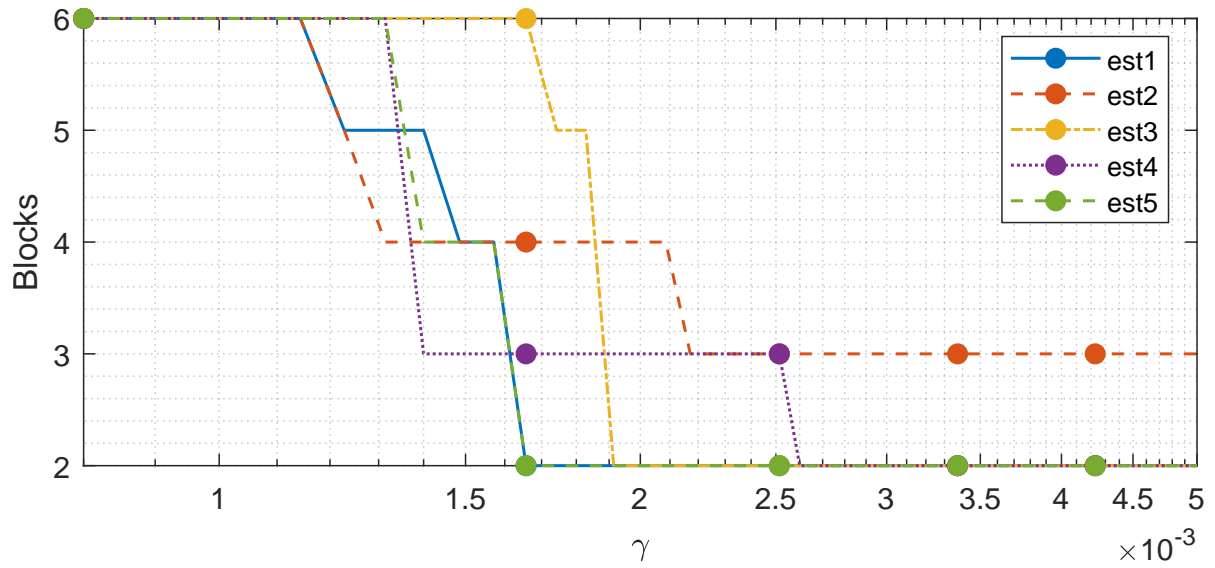
The scenario is run five times and only one of them does not achieve the actual number of sources as shown in Figure 13. Still, the two existing sources can be identified by visual inspection.

An important remark is that for the second experiment, a very uncommon result appears. The algorithm gets close to the true structure, but the does not achieve to find it exactly. Although, analysing the estimated sources, is clearly possible to identify the real sources and the third block estimated may be caused by the noise.

Motivated by the peaks in the frequency spectrum presented in Figure 14 and issues to generate structured signals with multiple poles but in narrow band. As recalled in Section 3, the literature shows that the rank of a Hankel matrix is equal to the number of poles present in the original signal. However, in experiments where the distance between poles is too short, more samples from the signal are necessary to find the rank equal the number of poles.

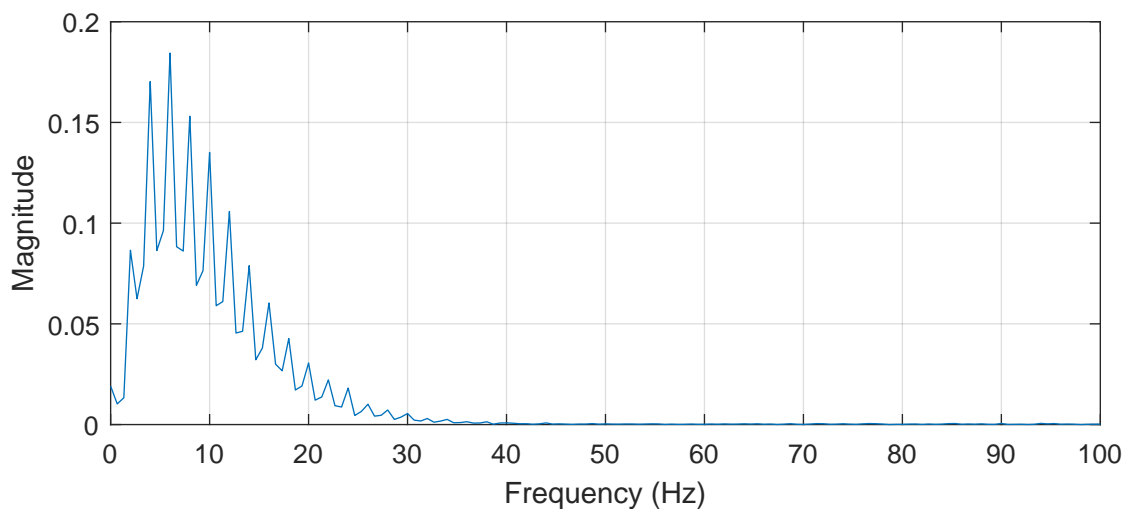
This complexity assessment of signals constructed from complex exponential sums structured as a Hankel matrix described above is presented in section 4.4.

Figure 13 – Number of blocks estimation for each γ in five CAGL runs.



Source: Prepared by the author.

Figure 14 – Semi-synthetic ECG single sided frequency spectrum (Welch's method).



Source: Prepared by the author.

4.3 Real ECG Scenario

This part of the work resulted in a published article in the conference *Computing in Cardiology* 2020, named **Tensor-Based Noninvasive Atrial Fibrillation Complexity Index For Catheter Ablation** (ABDALAH et al., 2020).

In order to propose a complexity index, CAGL is applied to estimate the AA sources, and based on its Hankel matrix rank, indicate how organized is the signal. It is a reasonable assumption to use it as complexity index since we can assume the ECG as a sum of exponentials, as the formulation in Section 3.3, and its relationship with the number of poles (M. GOULART et al., 2020), (DE LATHAUWER, 2011).

4.3.1 Tensor-Based AF Complexity Index

The complexity of a signal constructed from complex exponential sums is intrinsically related to the number of poles. Since the tensor block correlated with the AA signal presents a Hankel structure, its rank is equal to the number of poles (ZARZOSO, 2017). Therefore, the proposed AF complexity index is measured from the rank of the block that represents the atrial source.

4.3.2 Database and Experimental Setup

The present database consists in 59 ECG recordings from twenty male patients suffering from persistent AF, who had undergone step-wise CA that ended in procedural AF termination. All recordings belong to the Cardiology Department of Princess Grace Hospital Center, Monaco, acquired at a 977 Hz sampling rate and preprocessed by a zero-phase forward-backward type-II Chebyshev bandpass filter with cutoff frequencies of 0.5 and 40 Hz, in order to suppress high-frequency noise and baseline wandering.

Table 4 – Overall population characteristics.

Patient characteristics	Mean \pm (STD)	Min	Max
Age (years)	60.6 ± 9.4	42	76
Height (cm)	177.8 ± 6.2	169	195
Weight (kg)	85.6 ± 12.7	64	105
AF History (months)	68.6 ± 59.6	3	228
AF Episode (months)	16.3 ± 25.2	0.5	86
LA Diameter ² (mm)	45.8 ± 7.9	33	62

Source: Prepared by the author.

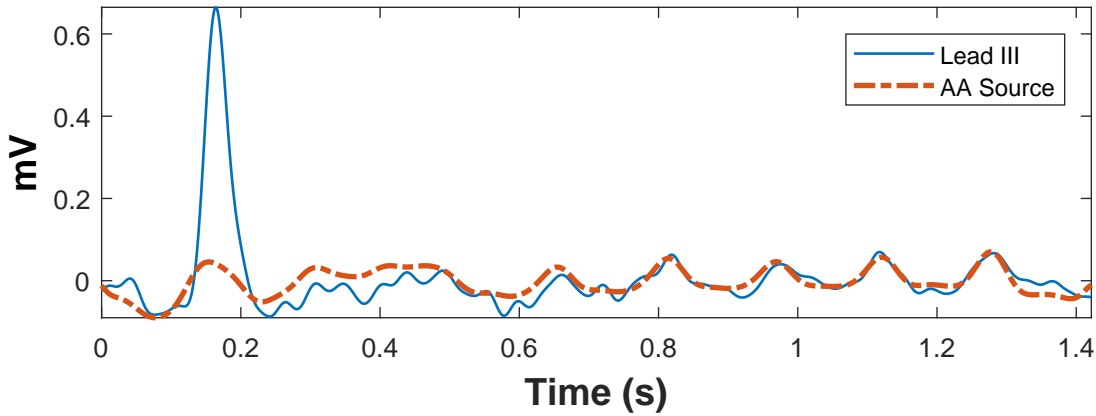
The Table 4 shows average age, height and weight, AF history, duration of the current AF episode (ongoing at the time of CA) and Left Atrium (LA) diameter.

²Missing data for one patient, the respective value was replaced by the mean.

The segment with the largest TQ segment is chosen for each patient, length range from 0.72 to 1.42 seconds. Since a window with the average length, 1.06 s, yields 1037 samples, a direct Hankelization of this matrix results in a tensor of dimensions 519 x 519 x 12, whose approximate BTD demands a large computing time. Therefore, we downsample the signals by a factor of 10 before apply the decomposition in order to reduce its computing time. The resulting tensor \mathcal{Y} have dimensions 52 x 53 x 12.

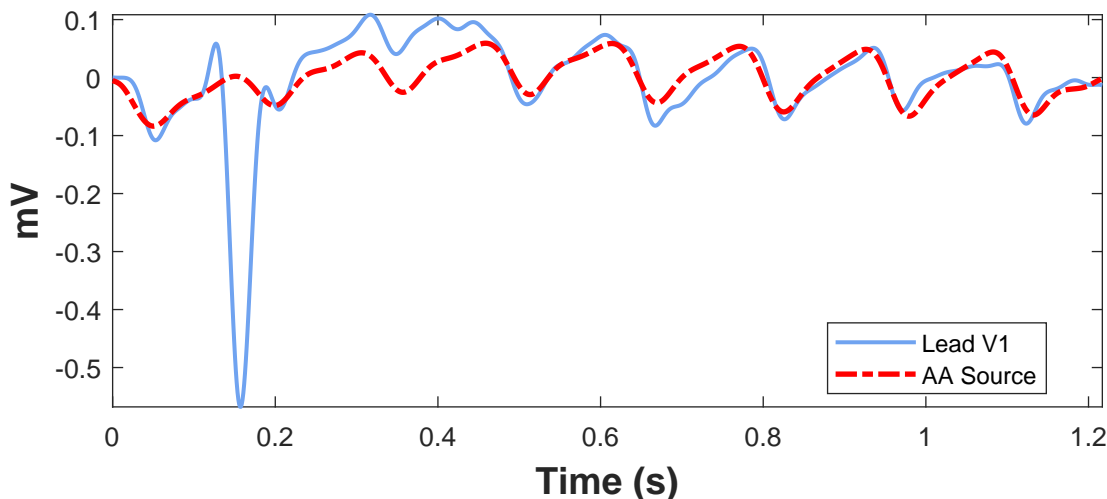
CAGL is applied to ECG recordings after each CA step, with a γ -sweeping procedure, inspired by solution-path techniques, with taking 50 equispaced values in the interval $[8 \times 10^{-4}, 0.5 \times 10^{-2}]$ and keeping the last solution. We start the algorithm with the initial guess of $R = 6$ and $L = 40$, from random blocks (M. GOULART et al., 2020).

Figure 15 – Example of AA block source with: SC = 63.5%, DF = 6.2 Hz, and kurtosis = 126.6.



Source: Prepared by the author.

Figure 16 – Example of AA block source with: SC = 74.3%, DF = 6.4 Hz, and kurtosis = 177.



Source: Prepared by the author.

Unfortunately, the task of measuring estimation quality is challenging since the

ground truth is unknown. However, some AA characteristics during AF can be exploited to guide selection of sources. The parameters used to assess AA extraction are spectral concentration (SC), dominant frequency (DF) and Kurtosis as well as visual inspection, with details in (DE OLIVEIRA; ZARZOSO, 2019), (MARINHO R. DE OLIVEIRA; ZARZOSO, 2018), (ZARZOSO; COMON, 2010). On this case, we assume that only one AA source exists and to the selection is based on which source maximize the SC defined (32),

$$\text{SC} = \left(\sum_{f_i=0.82f_p}^{1.17f_p} P_{AA}(f_i) \right) \left(\sum_{f_i=0}^{F_s/2} P_{AA}(f_i) \right)^{-1}, \quad (32)$$

where f_p is the value of the DF, defined as $\arg \max_{f_i} P_{AA}(f_i)$, F_s is the sampling frequency, f_i is the discrete frequency and P_{AA} is the power spectrum of the AA signal computed using Welch's method as in (CASTELLS et al., 2005). An AA signal during AF typically should have a DF between 3 and 9 Hz with high SC. Finally, the kurtosis of the signal in the frequency domain, acquired by a 4096-point FFT is computed as in (ZARZOSO; COMON, 2010). Since kurtosis measures peakedness and sparsity of a distribution, it consequently provides a quantitative measure of harmonicity of in the frequency domain of the computed signal. A high kurtosis is thus suggestive of a harmonic signal like AA during AF. An example of block that provide an atrial source estimation is shown in Figure 15.

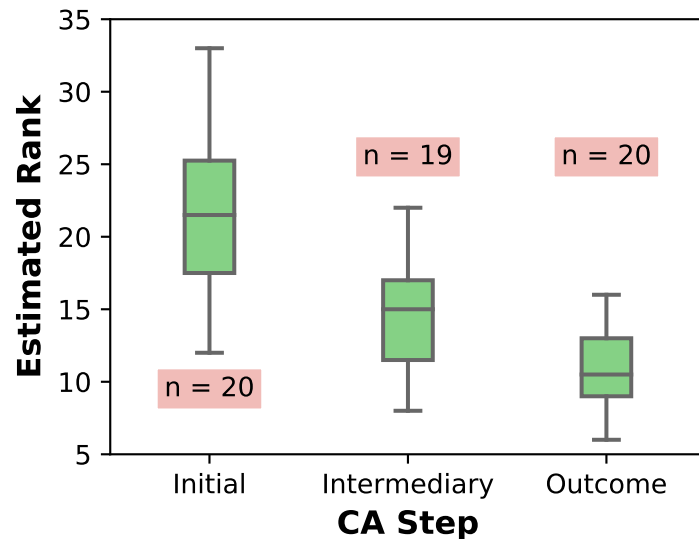
4.3.3 Catheter Ablation impact to Atrial Activity Complexity

The impact of CA at each step on AA complexity is assessed in terms of ranks estimation by CAGL in the whole dataset. Before any procedure, ranks range from 12 to 33, whereas after all steps of the CA procedure, ranks range from 6 to 16, referred to, respectively, as initial and outcome.

Initially, the population present a median rank 21.5, while at intermediaries steps is 15 and at procedures concluded it leads to 10.5, illustrating that such rank decreases at each step of the CA procedure as shown in Figure 17. This plot represents graphically depicts data through its quartiles, with boxes' edges represent the 25th and 75th percentiles, horizontal line in the middle of the box represents sample median and black whiskers represent the extreme data values that are not considered as outliers.

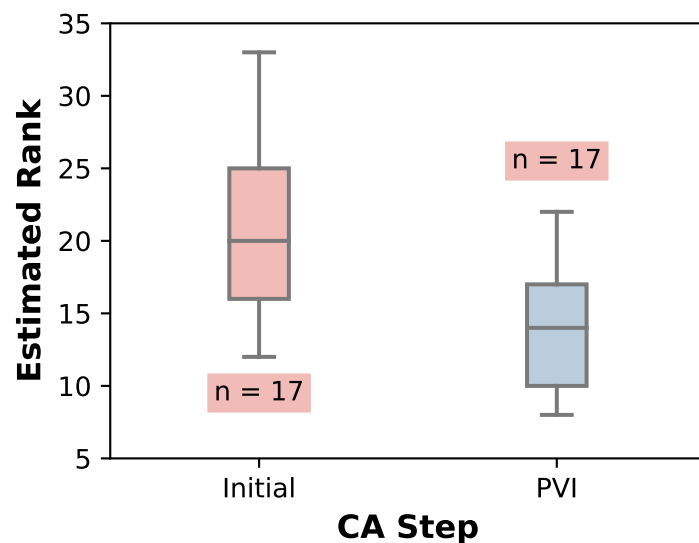
In observed segments, the rank of extracted AA sources becomes less complex as the ablation is performed as one could instinctively expect. In addition, a separate assessment of the 17 patients undergoing PVI is also shown in Figure 18. Presenting a drastic reduction of the proposed index after this CA step, from a median value of 20 to 14.

Figure 17 – Box-and-whisker plot showing the rank estimated by CAGL for all patients at different CA steps: initial (before ablation); intermediary (CA between the first and penultimate steps); outcome (after the last CA step). The n indicates the number of ECG segments in each box.



Source: Prepared by the author.

Figure 18 – Box-and-whisker plot at the beginning of CA and after PVI for the group of 17 patients who underwent this CA step.



Source: Prepared by the author.

4.3.4 Atrial Fibrillation Recurrence and Complexity

To assess population's features relationship, Pearson correlation (r) between the initial rank estimated by CAGL, i.e, before any patient had undergone CA procedure and AF recurrence, i.e, the time that each patient remained without AF episodes is -0.63 . A relevant value of negative correlation and well illustrated by its scattered data and linear regression in Figure 19, which seems to indicate an influence of initial rank on AF

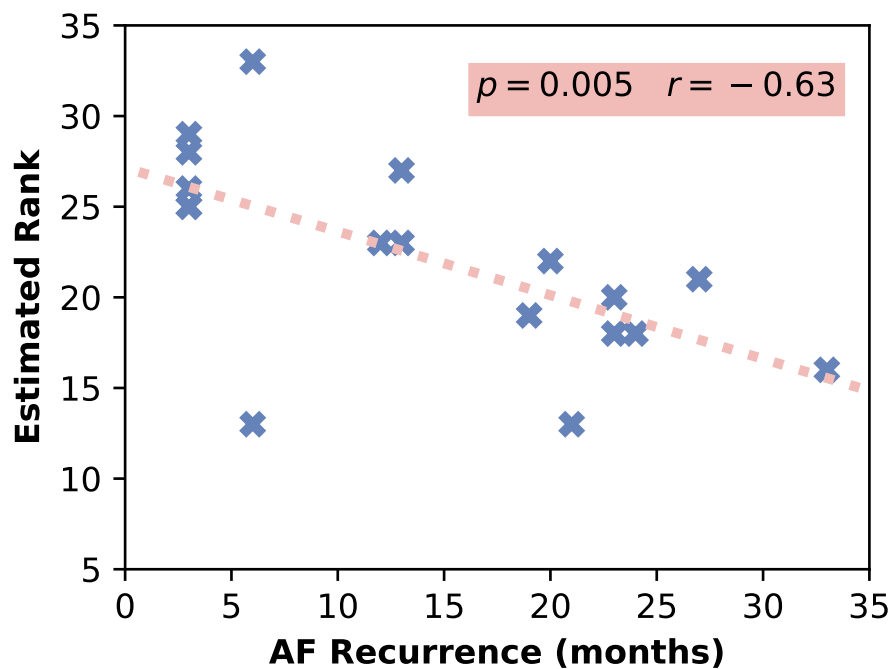
recurrence.

Based on its initial rank range two main clusters are identified, one composed of 6 patients who presented an AA rank between 25-33 before CA procedure had new AF episodes, while 1 presents rank 13, but presented AF recurrence in less than 6 months. While the other is composed of 10 patients with initial rank between 13-23, who remained in sinus rhythm for at least a year.

In addition, 2 patients don't fit the presented groups since the first one had 13 months without AF recurrence, despite a rank is 27, whereas the second can clearly be consider an outlier because its rank is 13, but presented AF recurrence in 6 months (the patient at the south-west in Figure 19, the furthest from the regression line).

Finally, 2 patients registered ranks 12 and 18 but have no information about AF recurrence after the CA procedure since they dropped out of the study, hence they were excluded from this assessment.

Figure 19 – Scatter plot of the initial estimated rank (before CA) of the block that provides the AA signal and AF recurrence. A negative correlation can be observed.



Source: Prepared by the author.

4.4 Hankel Signal Model

This part of the work resulted in a published article in the conference *XXXIX Simpósio Brasileiro de Telecomunicações e Processamento de Sinais* (2021), named **Low-Rank Hankel Signal Model: Numerical Results** (ABDALAH et al., 2021).

The experiments are divided in 3 scenarios. The first and second parts consider noiseless signals, whereas the third part is on noisy signals. In the first part we build a Vandermonde matrix from two vectors to illustrate how the distance between poles in the vector hamper the construction of a full-rank matrix, and consequently how it impacts the condition number, as theoretically anticipated in Section 3.6.

In the second part, we test various distances between poles to assess the minimum amount of samples necessary to obtain the Hankel matrix rank equal to the number of poles contained in the signal.

Finally, in the third scenario noisy signals are analyzed with various SNR values.

4.4.1 Condition Number

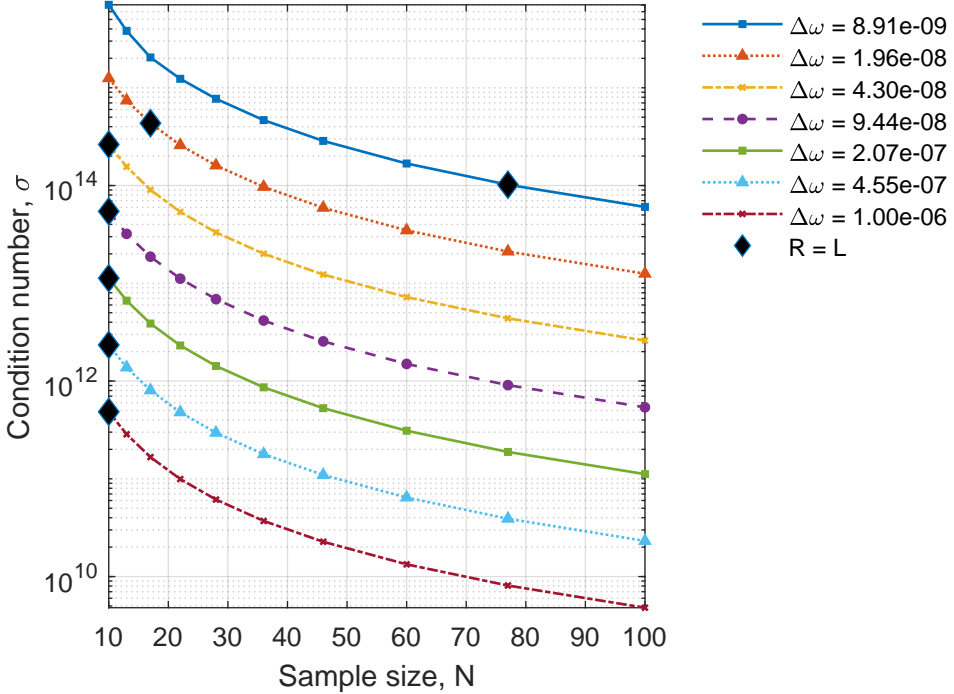
We assess the relationship between the condition number (σ) and the number of samples (N) varying the distance between the poles ($\Delta\omega$). An example inspired on the theoretical problem statement is assuming two vectors \mathbf{v}_1 and \mathbf{v}_2 as presented in Section 3.6, with $\omega_1 = 0$, and $\omega_2 = \Delta\omega$, i.e., $\mathbf{v}_1 = [1, 1, 1, \dots, 1]^\top$ and $\mathbf{v}_2 = [1, e^{j\Delta\omega}, e^{j2\Delta\omega}, \dots, e^{j(M-1)\Delta\omega}]^\top$, where \mathbf{v}_1 and \mathbf{v}_2 are the columns of the Vandermonde matrix \mathbf{V}_s . Hence, the Hankel matrix $\mathbf{H}_s \in \mathbb{C}^{N \times N}$ associated with this model is built from a simplified form of equation (5), where $\mathbf{V}_s \in \mathbb{C}^{N \times 2}$ and $\mathbf{D} \in \mathbb{R}^{2 \times 2}$ is an identity matrix. After constructing the Hankel matrix, we compute the SVD(\mathbf{H}_s) for 10 different values of N , rounding logarithmically spaced values in the interval $[10^1, 10^2]$, and considering 7 different values of $\Delta\omega$ as shown in Figure 20.

In the first place, if the distances between poles are so small, then even increasing the number of samples, σ keeps very high. This behavior affects rank computation and may prevent us to obtain $R = L$. Figure 20 also shows that σ decreases as we increase the number of samples to the columns, which compensates for the poles proximity as expected from the analysis of Section 3.6.

Moreover, for $\Delta\omega = [8.91 \times 10^{-9}, 1.96 \times 10^{-9}]$, σ indicates that $\lambda_1 \gg \lambda_2$ for all values of N , but it presents $R \neq L$ until reaching enough samples. Nevertheless, as N increases, σ tends to 1, i.e., the number of samples compensates for the insufficient distance between poles, allowing us to find $R = L$.

Finally, for other values of $\Delta\omega$, the condition number still indicates $\lambda_1 \gg \lambda_2$.

Figure 20 – Computing the condition number (σ) vs. the number of samples (N) to build the matrix using different values of $\Delta\omega$. For each curve, the diamond marker indicates the minimum value of N to have $\text{rank}(\mathbf{H}_s) = 2$.



Source: Prepared by the author.

However, with very few samples it is possible to find the rank (R) of \mathbf{H}_s equal to the number of poles L . It indicates that these are sufficient distances between poles.

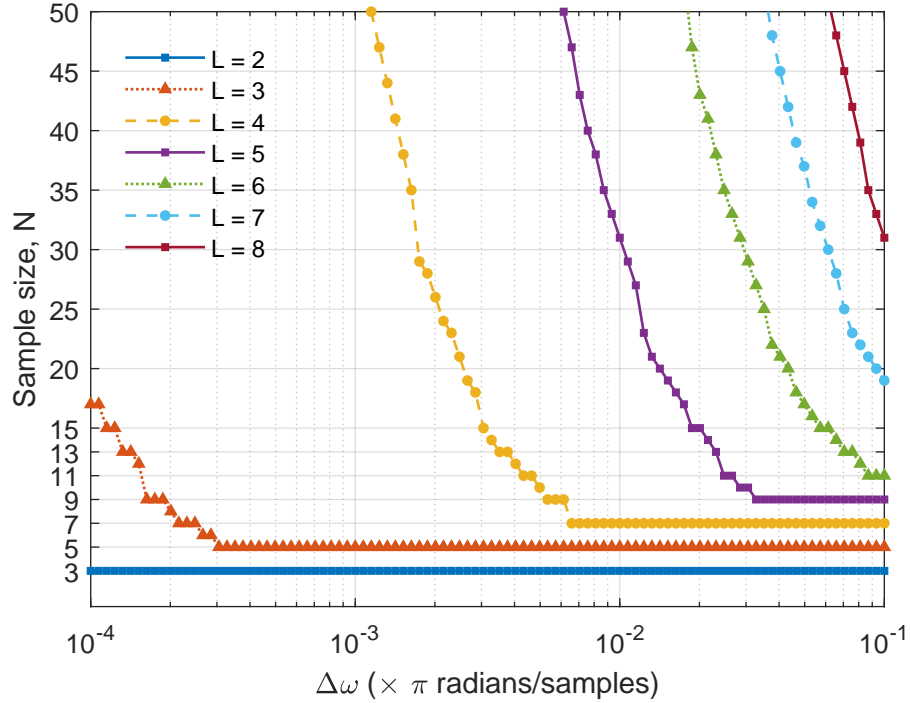
4.4.2 Sample Size for a Full-Rank Hankel Matrix

This scenario aims to assess how the poles proximity ($\Delta\omega$) in a signal $s(n)$ with L poles, shown in equation (3), impacts its Hankel matrix rank R in the absence of noise.

The experiment consists in constructing \mathbf{H}_s from 100 samples for each $s(n)$. To compare the numerical and theoretical results, we use a windowed version of $s(n)$ with $N \leq 100$ samples to build its equivalent Hankel structure, *i.e.*, just the window $s(1:N)$ from the first N samples, is used to map the signal onto the matrix. Then, we search through each \mathbf{H}_s mapped from the windowed signal for the first value of N yielding $R = L$.

We generate $s(n)$, where z_l represent equispaced poles, L is in the $[2,8]$ interval, and distance $\Delta\omega$ takes 100 logarithmically spaced values in the $[10^{-4}, 10^{-1}]$ interval. We assume that $c_l = 1$, $l = 1, 2, \dots, L$ for simplicity, but without loss of generality. The number of samples used in window N is a positive integer value between 2 and 100. The simulation of Figure 21 may be summarized as follows. For each value of L in the set of positive integers, we vary $\Delta\omega$ from very close poles gradually moving them away from each other at each iteration, noting the value of N for $R = L$.

Figure 21 – Number of samples N necessary to build a Hankel matrix \mathbf{H}_s , with $R = L$, versus the distance between poles ($\Delta\omega$). variation.



Source: Prepared by the author.

The experiment shows that the theoretical values based on equation (7) are different from those obtained empirically. One would expect plots with horizontal lines at $2L - 1$ regardless of $\Delta\omega$. Nevertheless, the simulation presents a different result: when the distance gets smaller, the number of samples N necessary in the windowed signal to build \mathbf{H}_s with $R = L$ increases. This outcome reinforces the hypothesis that the increase of N may compensate for the distance between poles to obtain $R = L$ as anticipated by the analysis of Section 3.6. This will increase the computational cost, since a reliable SVD algorithm (Golub-Reinsch) performs $8M^3/3$ flops to compute only the singular values (GOLUB; LOAN, 2013), where M is the matrix dimension following equation (4).

Furthermore, one can see that as L increases, the curves move towards top right corner of the figure, which suggests that rank depends on number of poles and $\Delta\omega$.

4.4.3 Noisy Scenario and SNR Threshold

To assess a more realistic case, one may consider a scenario with additive white Gaussian noise (AWGN), according to the following data model:

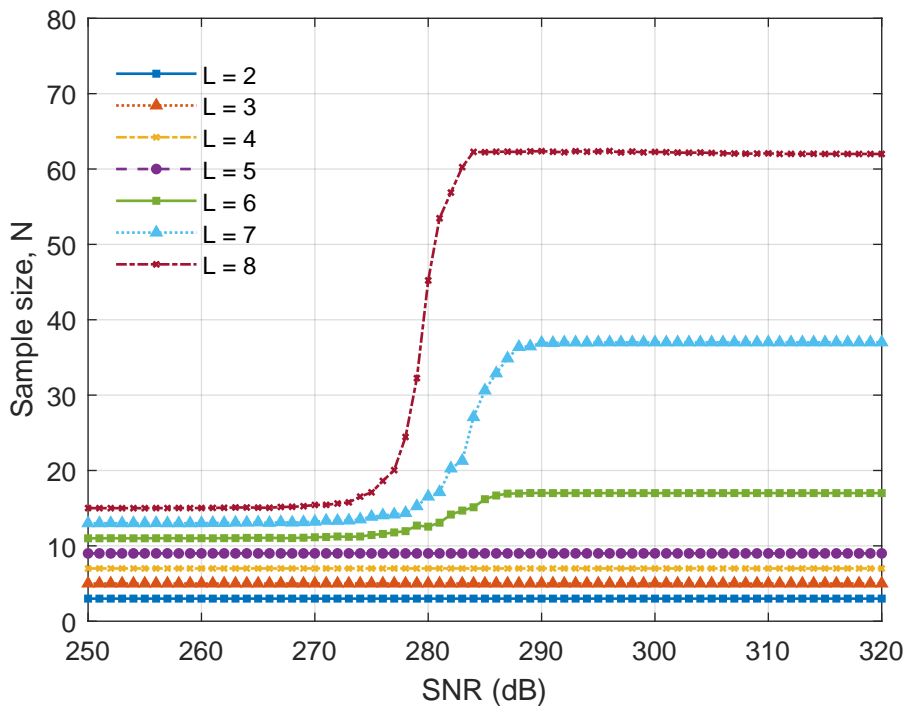
$$y(n) = s(n) + \beta(n). \quad (33)$$

The simulation framework setup is similar to the presented in Section 4.4.2, except

for the mapped signal $y(n)$, a version of $s(n)$ as shown in equation (3), affected by the AWGN term $\beta(n)$, and with a fixed distance between poles $\Delta\omega = 0.05$.

Aiming to compare the theoretical values based in equation (7) with the data obtained empirically, we present an experiment that varies high SNR values, along the [250,320] interval in 10 dB steps. The experiment is performed to search a threshold SNR value, where the equivalent Hankel matrix \mathbf{H}_s presents a rank R equal to the number of exponentials L , regardless of $\Delta\omega$. We repeat the procedure described in Section 4.4.2 (Figure 21) for each SNR, and noting the results obtained for each single run. The scenario with 100 Monte Carlo runs is computed varying the noise for each realization.

Figure 22 – Number of samples N necessary in the windowed signal $y(n)$ to build \mathbf{H}_s , with $R = L$, versus the SNR values, and fixed distance between poles $\Delta\omega = 0.05$ for 100 Monte Carlo runs.



Source: Prepared by the author.

Figure 22 shows that for values of SNR less than 270 dB, in general the most commonly encountered in real problems, the theoretical result is respected. The plots illustrate the expected result, discussed in previous sections, with horizontal lines at $2L - 1$, despite the $\Delta\omega$ variation with a rank R dependent only on its number of poles. For values greater than 270 dB, the theoretical values are once again different from those obtained empirically, but N starts to increase.

Finally, for this case of study, the three largest values of L present a transition close to 290 dB. We can see that for higher values of SNR, the trend observed in Figure 21 at $\Delta\omega = 0.05$ is exactly the same for all L . This outcome supports the results of Section 4.4.2, obtained in the noiseless case.

5 CONCLUSION

The present work discussion can be divided into understanding the problem formulation, using the tools to assess signals complexity, including ECG data, and exploring the numerical features of the low-rank Hankel signal model using Vandermonde decomposition. It explores various parameters as the distance between poles, and number of poles and samples in the construction of Hankel structures, mapped from all-pole signals. Since the initial goals were to use the tensor approach to propose a new complexity index to measure AA, one case say this objective was accomplished.

From the synthetic and semi-synthetic scenario, is possible to see the algorithm variability over its input parameter and how the tuning process is important to have good estimations even in scenarios where the ground-truth is well-known.

The main outcome from this work is the result presented in Section 4.3, that resulted on a published article named “Tensor-Based Noninvasive Atrial Fibrillation Complexity Index For Catheter Ablation” in the conference *Computing in Cardiology* 2020. Since from it, a novel index to noninvasively measure the AF complexity through step-wise CA procedure was proposed. This index results from CAGL algorithm for BTD computation, which have shown to be able to jointly extract the AA signal and measure the AF complexity from very short ECG recordings. In addition, experiments on a with the data set composed from 20 patients suffering from persistent AF have shown that the rank of the block that provides the AA signal decreases at each step of the CA procedure.

Also, a negative correlation between the estimated rank and AF recurrence was observed, a result that also can impact in clinical practice, since it can help to assess how effective will be the step-wise CA will be for each patient. In conclusion, this rank parameter could improve clinical analysis and support real-time guided CA, improving its accuracy, reducing cost and duration.

Furthermore, this work has also studied the numerical features of Hankel matrices associated with complex exponential signal models, with great outcomes presented Section 4.4, that resulted on a published article named “Low-Rank Hankel Signal Model: Numerical Results”, in the conference *Simpósio Brasileiro de Telecomunicações e Processamento de Sinais* 2021. We have that in the noiseless cases, to assure a full rank matrix and avoid the numerical problems presented, a minimum distance between poles is required or the number of mapped samples must increase to compensate for pole proximity and ensure full rank. These observations may impact the computational cost where the Vandermonde decomposition and Hankel structure are applied. In the noisy case, in real applications: with a realistic noise level, the Hankel matrix is always full rank, since the noise acts to balance the linear independence between the columns in the associated Vandermonde matrix. This can reduce significantly the computational cost for problems with solid

ground-truth.

Experiments based on the SVD measure the impact of parameters, taking into consideration two indices: the condition number, and the amount of samples mapped onto a Hankel matrix necessary to present a rank equal to the number poles in the equivalent signal. An unexpected relationship between the parameters appears in the noiseless case due to numerical effects, despite the noisy setup that presents the expected behavior with a limited SNR. Also, evidence was given with the help of simulations to support two remarks:

- (I) As the distance between poles decreases, the number required to obtain a full rank matrix increases. Furthermore, in the second noiseless scenario, with a low-rank Hankel signal model, if the poles get too close to each other, a dependency between the rank, number of poles, amount of samples, and the distance between poles is observed.
- (II) In the noisy scenario, with SNR values commonly encountered in practice, the distance between poles becomes irrelevant. The theoretical minimum value is observed, *i.e.*, the rank depends only on the number of poles.

5.1 Further Work

Future work should focus on comparing the proposed index with other indices in the literature and performing experiments in a larger database of patient, in order to provide more relevant clinical results. Also exploring the optimal choice for tuning (γ, τ) parameters for both AGL and CAGL.

In addition, in the low-rank Hankel signal model part, further research should shed light on performing the condition number experiment for larger Vandermonde matrices, in order to compare more than two singular values to provide more relevant statistical information. Furthermore, the experiments should be in the context of tensor decompositions, such as BTD, since the model performs the separation of the noise in a different block of the low-rank Hankel signal model and the remaining blocks could fall within the noiseless scenario.

REFERENCES

- ABDALAH, L.; OLIVEIRA, P. M. R. de; FREITAS, W.; ZARZOSO, V. Low-Rank Hankel Signal Model: Numerical Results. In: XXXIX Simpósio Brasileiro de Telecomunicações e Processamento de Sinais. Fortaleza, Brazil, Sept. 2021.
- ABDALAH, L.; OLIVEIRA, P. M. R. de; FREITAS, W.; ZARZOSO, V. Tensor-Based Noninvasive Atrial Fibrillation Complexity Index For Catheter Ablation. In: COMPUTING in Cardiology. Rimini, Italy, Sept. 2020.
- AMBESH, P.; KAPOOR, A. Biological pacemakers: Concepts and techniques. **The National Medical Journal of India**, v. 30, p. 324, Nov. 2017.
- BECKERMANN, B.; GOLUB, G.; LABAHN, G. On the numerical condition of a generalized Hankel eigenvalue problem. **Numerische Mathematik**, v. 106, p. 41–68, 2007.
- BOLEY, D.; LUK, F.; VANDEVOORDE, D. A General Vandermonde Factorization of a Hankel Matrix. **Int. Lin. Alg. Soc.(ILAS) Symp. on Fast Algorithms for Control, Signals and Image Processing**, 1997.
- BRUNTON, S. L.; KUTZ, J. N. Singular Value Decomposition (SVD). In: DATA-DRIVEN Science and Engineering: Machine Learning, Dynamical Systems, and Control. Cambridge University Press, 2019. p. 3–46.
- CADZOW, J. A. Signal enhancement-a composite property mapping algorithm. **IEEE Transactions on Acoustics, Speech, and Signal Processing**, v. 36, n. 1, p. 49–62, 1988.
- CARDOSO, J. Blind signal separation: statistical principles. **Proceedings of the IEEE**, v. 86, n. 10, p. 2009–2025, 1998.
- CASTELLS, F.; RIETA, J. J.; MILLET, J.; ZARZOSO, V. Spatiotemporal blind source separation approach to atrial activity estimation in atrial tachyarrhythmias. **IEEE Transactions on Biomedical Engineering**, v. 52, n. 2, p. 258–267, 2005.
- DE LATHAUWER, L. Blind Separation of Exponential Polynomials and the Decomposition of a Tensor in Rank- $(L_r, L_r, 1)$ Terms. **SIAM Journal on Matrix Analysis and Applications**, v. 32, n. 4, p. 1451–1474, 2011.
- DE OLIVEIRA, P. M. R.; ZARZOSO, V. Block Term Decomposition of ECG Recordings for Atrial Fibrillation Analysis: Temporal and Inter-Patient Variability. **Journal of Communication and Information Systems**, v. 34, p. 111–119, 2019.
- GOLUB, G. H.; LOAN, C. F. van. **Matrix Computations**. Fourth ed.: John Hopkins University Press, 2013.
- HAÏSSAGUERRE, M.; JAÏS, P.; SHAH, D. C.; TAKAHASHI, A.; HOCINI, M., et al. Spontaneous Initiation of Atrial Fibrillation by Ectopic Beats Originating in the Pulmonary Veins. **New England Journal of Medicine**, v. 339, n. 10, p. 659–666, 1998.
- JANUARY, C. T.; WANN, L. S.; ALPERT, J. S.; CALKINS, H.; CIGARROA, J. E., et al. 2014 AHA/ACC/HRS guideline for the management of patients with atrial fibrillation: A report of the American College of Cardiology/American Heart Association Task Force on practice guidelines and the Heart Rhythm Society. **Circulation**, v. 64, n. 21, p. 2246–2280, Dec. 2014.

- KIRCHHOF, P.; CALKINS, H. Catheter ablation in patients with persistent atrial fibrillation. **European Heart Journal**, v. 38, n. 1, p. 20–26, July 2016.
- M. GOULART, J. H. de; DE OLIVEIRA, P. M. R.; FARIAS, R. C.; ZARZOSO, V.; COMON, P. Alternating Group Lasso for Block-Term Tensor Decomposition and Application to ECG Source Separation. **IEEE Transactions on Signal Processing**, v. 68, p. 2682–2696, 2020.
- M. R. DE OLIVEIRA, P.; ZARZOSO, V. Block Term Decomposition of ECG Recordings for Atrial Fibrillation Analysis: Temporal and Inter-Patient Variability. **Journal of Communication and Information Systems**, v. 34, n. 1, p. 111–119, 2019.
- MAINARDI, L.; SÖRNMO, L.; CERUTTI, S. **Understanding Atrial Fibrillation: The Signal Processing Contribution**. Morgan & Claypool Publishers, 2008.
- MARINHO R. DE OLIVEIRA, P.; ZARZOSO, V. Source Analysis and Selection Using Block Term Decomposition in Atrial Fibrillation. In: 14TH International Conference on Latent Variable Analysis and Signal Separation (LVA/ICA 2018). Guildford, United Kingdom, July 2018. (Latent Variable Analysis and Signal Separation), p. 46–56.
- RIBEIRO, L. N.; HIDALGO-MUÑOZ, A. R.; ZARZOSO, V. Atrial signal extraction in atrial fibrillation electrocardiograms using a tensor decomposition approach. In: 2015 37th Annual International Conference of the IEEE Engineering in Medicine and Biology Society (EMBC). 2015. p. 6987–6990.
- RIETA, J. J.; CASTELLS, F.; SANCHEZ, C.; ZARZOSO, V.; MILLET, J. Atrial activity extraction for atrial fibrillation analysis using blind source separation. **IEEE Transactions on Biomedical Engineering**, v. 51, n. 7, p. 1176–1186, 2004.
- RIETA, J. J.; CASTELLS, F.; SÁNCHEZ, C.; ZARZOSO, V.; MILLET, J. Atrial Activity Extraction For Atrial Fibrillation Analysis Using Blind Source Separation. **IEEE Transactions on Biomedical Engineering**, v. 51, n. 7, p. 1176–1186, 2004.
- SEITZ, J.; BARS, C.; THÉODORE, G.; BEURTHERET, S., et al. AF Ablation Guided by Spatiotemporal Electrogram Dispersion Without Pulmonary Vein Isolation: A Wholly Patient-Tailored Approach. **Journal of the American College of Cardiology**, v. 69, n. 3, p. 303–321, 2017.
- STRIDH, M.; SÖRNMO, L. Spatiotemporal QRST cancellation techniques for analysis of atrial fibrillation. **IEEE Transactions on Biomedical Engineering**, v. 48, n. 1, p. 105–111, 2001.
- WALL, M. E.; RECHTSTEINER, A.; ROCHA, L. M. Singular Value Decomposition and Principal Component Analysis. In: **A Practical Approach to Microarray Data Analysis**. Ed. by D.P. Berrar, W. Dubitzky and M. Granzow. 2003. p. 91–109.
- WERUAGA, L.; AL-KHAYAT, A. All-pole model estimation of vocal tract on the frequency domain. **Proceedings of the Annual Conference of the International Speech Communication Association**, v. 2, 2006.
- YUAN, M.; LIN, Y. Model selection and estimation in regression with grouped variables. **Journal of the Royal Statistical Society: Series B (Statistical Methodology)**, v. 68, n. 1, p. 49–67, 2006.

ZARZOSO, V.; COMON, P. Robust Independent Component Analysis by Iterative Maximization of the Kurtosis Contrast With Algebraic Optimal Step Size. **IEEE Transactions on Neural Networks**, v. 21, n. 2, p. 248–261, 2010.

ZARZOSO, V. Extraction of ECG Characteristics Using Source Separation Techniques: Exploiting Statistical Independence and Beyond. In: NAIT-ALI, A. (Ed.). **Advanced Biosignal Processing**. Springer, 2009. chap. 2, p. 15–47.

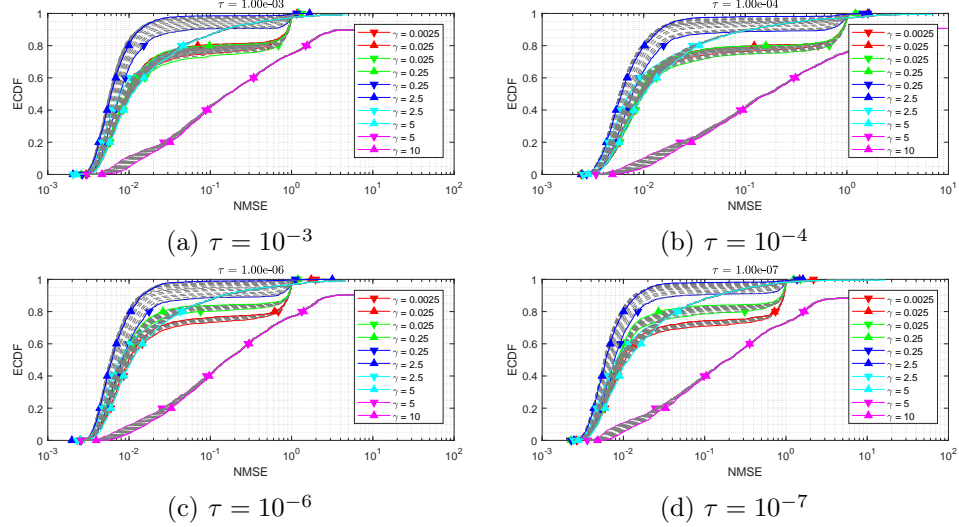
ZARZOSO, V. Extraction of ECG characteristics using source separation techniques: exploiting statistical independence and beyond. In: ADVANCED BIOSIGNAL PROCESSING. 2009. p. 15–48.

ZARZOSO, V. Parameter estimation in block term decomposition for noninvasive atrial fibrillation analysis. In: 2017 IEEE 7th International Workshop on Computational Advances in Multi-Sensor Adaptive Processing (CAMSAP). Dec. 2017. p. 1–5.

APPENDIX A - FURTHER RESULTS

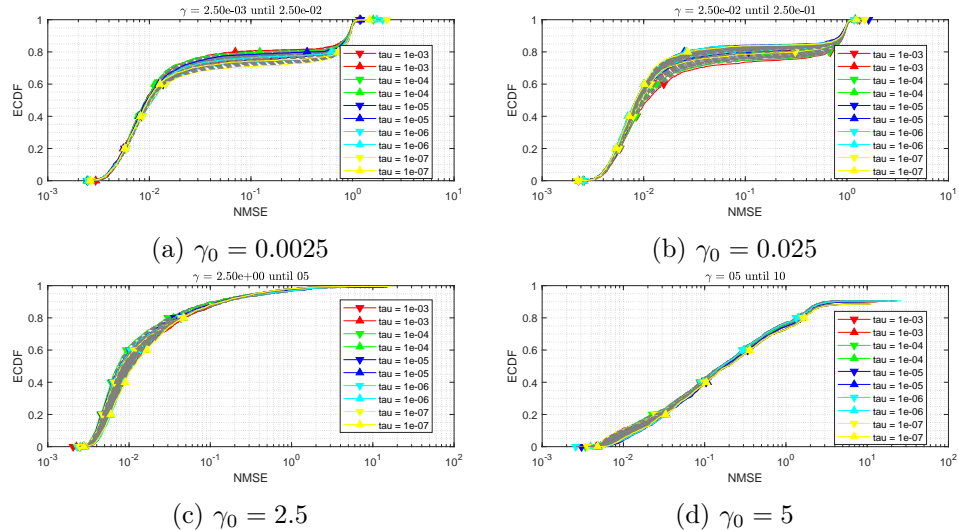
In order to reinforce AGL's robustness to τ , recalling Section 4.1, this following experiment are shown exploring further parameters values for both τ and γ .

Figure 23 – Further results of experiments from Figure 10 (a), but with different values for τ , as shown on subtitle.



Source: Prepared by the author.

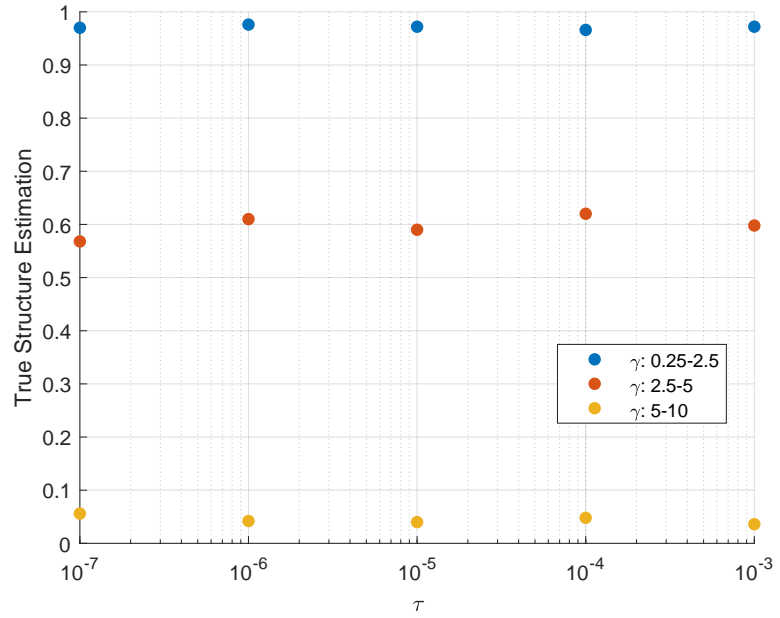
Figure 24 – Further results of experiments from Figure 10 (b), but with different values for γ_0 , as shown on subtitle.



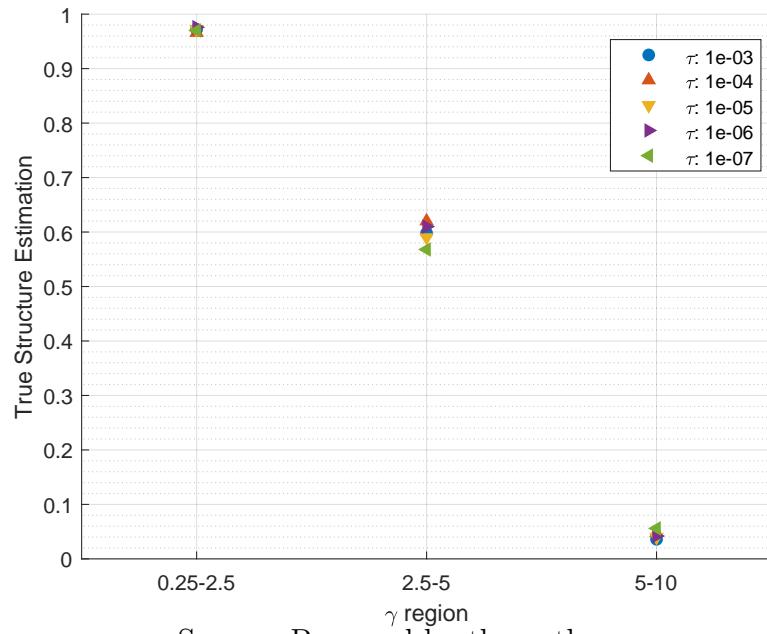
Source: Prepared by the author.

Figure 25 – Scatter plot describing the rate of true structure estimation for each τ , and each color represents a γ -region.

(a) Scatter plot describing the rate of true structure estimation for different regions of γ -sweeping. The legend indicates τ .



(b) Scatter plot describing the rate of true structure estimation for different τ . The legend indicates the region of γ -sweeping.



Source: Prepared by the author.

APPENDIX B - RELATED PUBLICATIONS

Published papers with the main results of this work.

Tensor-Based Noninvasive Atrial Fibrillation Complexity Index For Catheter Ablation

Lucas de S Abdalah^{1,2}, Pedro Marinho R de Oliveira¹, Walter Freitas Jr², Vicente Zarzoso¹

¹ Université Côte d'Azur, CNRS, I3S Laboratory, Sophia Antipolis, France

² Universidade Federal do Ceará, Fortaleza, Brazil

Abstract

Due to the cost-efficiency of the ECG, the interest in noninvasive techniques to assess atrial fibrillation (AF) electrophysiological complexity is increasingly high. Still, ECG-based methods to measure AF complexity are limited in clinical practice and need estimation of the atrial activity (AA) signal from sufficiently long ECG recordings. The present work proposes an algorithm for tensor decomposition called constrained alternating group lasso (CAGL) as a noninvasive tool to quantify AF complexity. Experiments with a database of 59 ECG recordings from 20 patients suffering from persistent AF show that CAGL is able to both extract the AA and quantify its complexity from very short ECG recordings (1.06 ± 0.20 s). All the patients had undergone step-wise catheter ablation (CA) that ended in procedural AF termination. CAGL is applied on the ECG recording before CA and at each step procedure, measuring the rank of the tensor that provides the AA signal. It is observed that such rank decreases at each step of the CA procedure, showing a less complex AA signal as the ablation is performed. A statistical correlation between AA complexity measured by the new index and AF recurrence after CA is observed. The proposed index is a potential tool to guide CA procedures in real time.

1. Introduction

Atrial fibrillation (AF) is the most frequent sustained arrhythmia encountered in clinical practice, responsible for an increasingly high number of hospitalizations and deaths [1]. This challenging cardiac condition is known as the last great frontier in cardiac electrophysiology, as the electrophysiological mechanisms responsible for its triggering and maintenance are not completely understood. A noninvasive and cost-effective way to study this cardiac rhythm disorder is analyzing the atrial activity (AA) signal from the standard 12-lead electrocardiogram (ECG). However, the AA during AF is characterized by low-amplitude fibrillatory waves, called f-waves, that are masked by the

QRS complex responsible for the ventricular activity (VA) in each heartbeat. In addition, the AA sometimes presents an amplitude lower than the noise, hampering its analysis [2].

During AF, the AA and the VA signals are typically assumed uncoupled, so that the extraction of AA from the ECG admits a blind source separation (BSS) formulation [3]. The block-term decomposition (BTD) built from Hankel matrices, proposed as a technique to solve BSS problems in [4], was used to noninvasively extract the AA signal from AF ECG recordings, showing that it can outperform the matrix-based techniques in this particular application [5], [6].

Step-wise catheter ablation (CA) is an effective therapy to treat persistent AF and restore sinus rhythm [7]. Hence, methods to measure AA complexity at each procedural step are relevant to improve clinical analysis and guide CA in real time. Furthermore, it would be desirable to clarify the impact on AF of each intervention step such as pulmonary vein isolation (PVI) and other widely used techniques [8], [9]. However, existing methods for noninvasive quantification of AF complexity are limited due to the fact that sufficiently long ECG recordings are required, hindering their use in clinical practice.

Aiming to overcome such limitations, the present work introduces a recently proposed algorithm to compute the BTD, called CAGL [10], as an AF complexity index. CAGL is able to jointly extract the AA signal from the ECG and measure AF complexity from very short recordings (1.06 ± 0.20 s). The AF complexity is measured from the rank of the tensor block associated with the AA signal.

2. Methods

2.1. Block Term Decomposition

An ECG recording from K leads composed by N time samples can be modeled as a matrix factorization:

$$\mathbf{Y} = \mathbf{MS} \in \mathbb{R}^{K \times N} \quad (1)$$

where $\mathbf{M} \in \mathbb{R}^{K \times R}$ is the mixing matrix, modeling the propagation of the cardiac electrical sources from the heart

to the body surface, $\mathbf{S} \in \mathbb{R}^{R \times N}$ is the source matrix that contains mainly the atrial and ventricular sources and R is the number of sources [3]. Nevertheless, matrix-based methods impose constraints that may lack physiological grounds. In this case, we propose a tensor approach using Hankel-BTD model that outperform matrix-based techniques under much milder constraints [4], [10].

A tensor is an extension of the matrix concept. While matrices are two-dimensional arrays, a third-order tensor $\mathcal{Y} \in \mathbb{R}^{I \times J \times K}$ is a three-dimensional array, whose BTD is written as:

$$\mathcal{Y} = \sum_{r=1}^R (\mathbf{A}_r \mathbf{B}_r^\top) \circ \mathbf{x}_r \quad (2)$$

where $\mathbf{A}_r \in \mathbb{R}^{I \times L_r}$ and $\mathbf{B}_r \in \mathbb{R}^{J \times L_r}$ are the factors matrices, and have rank L_r . The symbols $(\cdot)^\top$ and \circ denote the transposition operator, and the outer product, respectively.

The Hankel-BTD method suits the characteristics of AA in AF episodes. Due to the quasi-periodic nature of AF signals, atrial sources can be well represented by an all-pole model, *i.e.*, a sum of complex exponentials [11]. Hence, each ECG lead can be mapped onto a Hankel matrix, and these matrices are stacked in a third-order tensor $\mathcal{Y}_{\mathcal{H}}$, as described in [4], [6], that admits the following model:

$$\mathcal{Y}_{\mathcal{H}} = \sum_{r=1}^R \mathbf{H}_{\mathbf{S}}^{(r)} \circ \mathbf{m}_{\cdot r} \quad (3)$$

where $\mathbf{H}_{\mathbf{S}}^{(r)}$ is a Hankel matrix built from the r^{th} source of \mathbf{S} , and $\mathbf{m}_{\cdot r}$ is the r^{th} mixing matrix column.

2.2. Constrained Alternating Group Lasso

In general, an approximate BTD is computed by minimizing the Euclidean distance between the observed data tensor $\mathcal{Y} \in \mathbb{C}^{I \times J \times K}$ and a model of fixed structure with respect to the model components:

$$f(\mathbf{A}, \mathbf{B}, \mathbf{X}) \triangleq \left\| \mathcal{Y} - \sum_{r=1}^R (\mathbf{A}_r \mathbf{B}_r^\top) \circ \mathbf{x}_r \right\|_F^2. \quad (4)$$

In the special case of interest, \mathbf{H}_r must belong to the subspace of Hankel matrices with dimensions $(I \times J)$, denoted $\mathcal{S}_{\mathcal{H}}$. The mode-3 slices $\mathbf{Y}_{\cdot \cdot k}$ of the observed tensor are Hankel by construction. However, a solution $(\hat{\mathbf{A}}, \hat{\mathbf{B}}, \hat{\mathbf{X}})$ of (4) may not satisfy $\hat{\mathbf{A}}_r \hat{\mathbf{B}}_r^\top \in \mathcal{S}_{\mathcal{H}}$, due to noise and modeling imperfections. Also, algorithms based on (4) are strongly dependent of the initialization of its matrix factors and do not estimate the model parameters, *i.e.*, the number of blocks and their ranks.

To overcome such limitations, instead of using a fixed BTD structure as in (4), an algorithm called AGL and its constrained version described for Hankel matrices called

CAGL are proposed in [10]. This method includes penalization terms promoting low-rank blocks and controlling the number of blocks, yielding criteria of the form:

$$F(\mathbf{A}, \mathbf{B}, \mathbf{X}) \triangleq f(\mathbf{A}, \mathbf{B}, \mathbf{X}) + \gamma g(\mathbf{A}, \mathbf{B}, \mathbf{X}) \quad (5)$$

where $\gamma > 0$ is a regularization parameter and g is a regularization function of the form:

$$g(\mathbf{A}, \mathbf{B}, \mathbf{X}) \triangleq \|\mathbf{A}\|_{2,1} + \|\mathbf{B}\|_{2,1} + \|\mathbf{X}\|_{2,1}. \quad (6)$$

Notation $\|\cdot\|_{2,1}$ denotes the mixed $\ell_{2,1}$ -norm, *i.e.*, the sum of ℓ_2 norms of the columns of its matrix argument. Due to the geometric properties of the mixed $\ell_{2,1}$ -norm, solutions where \mathbf{A} , \mathbf{B} and \mathbf{X} have null columns (for sufficiently high γ values) will be induced, allowing one to select the relevant low-rank blocks. This method is called group lasso and is a generalization of the the lasso estimator principle [12].

In order to ensure the Hankel structure of the matrix factors at the end of iterations, a structured low-rank approximation is applied at convergence of the algorithm, yielding CAGL. For this purpose, the Cadzow's Algorithm [13] is used at the end of the iterations, which consists in performing alternating projections onto the Hankel subspace $\mathcal{S}_{\mathcal{H}}$, so that $\hat{\mathbf{H}}_r \approx \hat{\mathbf{A}}_r \hat{\mathbf{B}}_r^\top \in \mathcal{S}_{\mathcal{H}}$. A detailed description of the CAGL algorithm can be found in [10].

2.3. Tensor-Based AF Complexity Index

The complexity of a signal constructed from complex exponential sums is intrinsically related to the number of poles. Since the tensor block correlated with the AA signal presents a Hankel structure, the rank of its matrix factor L_r is equal to the number of poles [5]. Therefore, the proposed index is measured from the rank of the block that represents the atrial source, that allows a more global view of what goes on in the atria, while a catheter provides more local information.

2.4. Database and Experimental Setup

The present database consists in 59 ECG recordings from 20 patients suffering from persistent AF, who had undergone step-wise CA that ended in procedural AF termination. All recordings belong to the Cardiology Department of Princess Grace Hospital Center, Monaco, acquired at a 977 Hz sampling rate. They are preprocessed by a zero-phase forward-backward type-II Chebyshev bandpass filter with cutoff frequencies of 0.5 and 40 Hz, in order to suppress high-frequency noise and baseline wandering.

Twenty male patients compose the population with average age, height and weight, respectively, of 60.6 ± 9.4 years, 177.8 ± 6.2 cm and 85.6 ± 12.7 kg. Left atrium¹

¹The value for one patient was replaced by the mean.

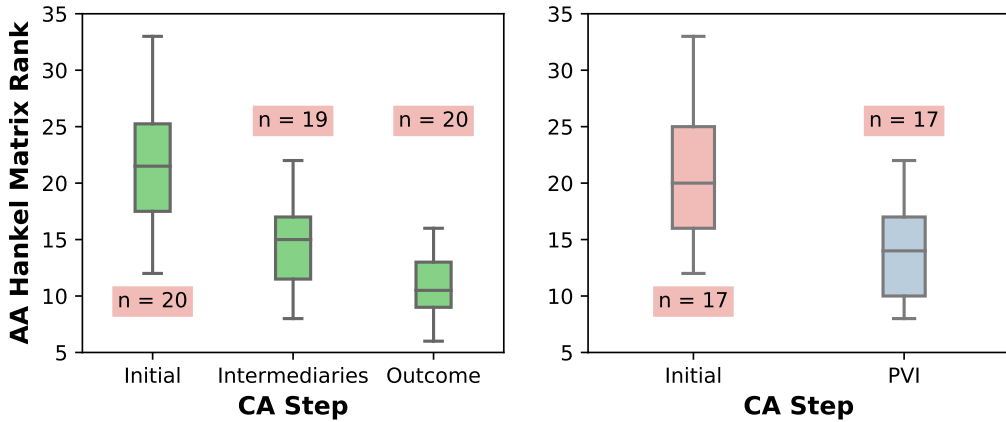


Figure 1. Right: Box-and-whisker plot showing the rank estimated by CAGL for all patients at different CA steps: initial (before ablation); intermediaries (CA between the first and penultimate steps); outcome (after the last CA step). Left: Box-and-whisker plot at the beginning of CA and after PVI for the group of 17 patients who underwent this CA step. Notation (n) indicates the number of ECG segments considered in each box.

diameter was 45.8 ± 7.9 mm. In addition, AF history was of 68.6 ± 59.6 months, while duration of the current AF episode (ongoing at the time of CA) was 16.3 ± 25.2 months.

The segment with the largest TQ segment is chosen for each patient, length ranging from 0.72 to 1.42 seconds. A window with length 1.06 s, yields 1037 samples, a direct row-Hankelization of this matrix results in a tensor of dimensions $519 \times 519 \times 12$, whose approximate BTD demands a large computing time. Therefore, we downsample the signals by a factor of 10 before apply the decomposition in order to reduce its computing time, with practically negligible information loss. In this example, the resulting tensor \mathcal{Y} have dimensions $52 \times 53 \times 12$.

CAGL is applied to ECG recordings after each CA step, with a γ -sweeping procedure, inspired by solution-path techniques, by taking 50 equispaced values in the interval $[8 \times 10^{-4}, 0.5 \times 10^{-2}]$ and keeping the last solution. We start the algorithm with $R = 6$ random blocks and rank $L_r = 40$ as initial guess [10]. The task of measuring estimation quality is challenging since the ground truth is unknown. Nevertheless some AA characteristics during AF must be exploited to guide sources selection. The parameters used to evaluate AA extraction are spectral concentration (SC), dominant frequency (DF) and kurtosis as well as visual inspection, as detailed in [6], [14], [15].

3. Experimental Results

3.1. AA Complexity influence by PVI

The impact of CA at each step on AA complexity is assessed in terms of rank estimation by CAGL in the whole dataset. Before CA, ranks range from 12 to 33, whereas

after all steps of the CA procedure, ranks range from 6 to 16, referred to, respectively, as ‘Initial’ and ‘Outcome’ in Figure 1. Initially, the population present a median rank 21.5, while at intermediaries steps is 15 and after CA it becomes 10.5, illustrating that the rank decreases at each step of the CA procedure as shown in Figure 1. This plot graphically depicts data through their quartiles, with boxes’ edges represent the 25th and 75th percentiles, horizontal line in the middle of the box represents sample median and black whiskers represent the extreme data values that are not considered as outliers.

In observed segments, the rank of extracted AA sources becomes less complex as the ablation is performed as one could intuitively expect. In addition, a separate assessment of the 17 patients undergoing PVI is also shown in Figure 1, presenting a drastic reduction of the proposed index after this CA step, from a median value of 20 to 14.

3.2. AF Recurrence and Complexity

To assess the relationship between population’s features, Pearson correlation (r) between the initial rank estimated by CAGL, *i.e.*, before any patient had undergone CA procedure, and AF recurrence, *i.e.*, the time that each patient remained in sinus rhythm before AF relapse is -0.63 . A statistical relevant value of negative correlation well illustrated by its scatter plot and linear regression in Figure 2, seems to indicate an influence of initial rank on AF recurrence.

Finally, 2 patients registered ranks 12 and 18 but had no information about AF recurrence after the CA procedure, since they dropped out of the study. Hence, they were excluded from this assessment.

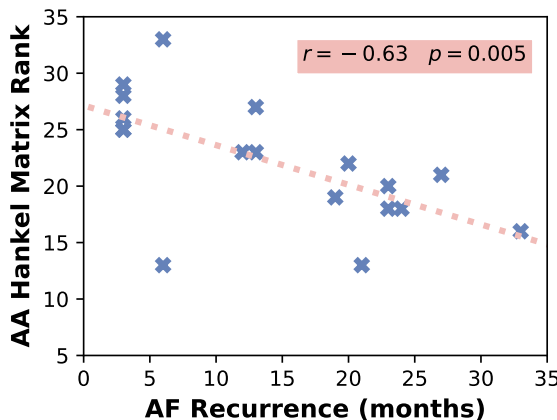


Figure 2. Scatter plot of the initial estimated rank (before CA) of the tensor block that provides the AA signal versus AF recurrence. A negative correlation can be observed.

4. Conclusions

The present work proposed a novel index to noninvasively measure the AF complexity using tensor models. This index is based on the CAGL algorithm for BTD computation, which is able to jointly extract the AA signal and measure AF complexity from very short ECG recordings. Experiments on a database of 20 AF patients have shown that the rank of the block that provides the AA signal decreases at each step of the CA procedure. Also, it was observed a negative correlation between the estimated rank and AF recurrence. In conclusion, this rank parameter could improve clinical analysis and support real-time guided CA, improving its accuracy, while reducing its cost and duration.

Future work should focus on comparing the proposed complexity parameter with other state-of-the-art indices and performing experiments in a larger database of patients in order to provide more relevant clinical results.

Acknowledgments

Lucas de S. Abdalah is supported by the BRAFITEC program at Université Côte d’Azur, financed by CAPES within the Ministry of Education of Brazil. Pedro Marinho R. de Oliveira is funded by a PhD scholarship from the IT Doctoral School (ED STIC) of the Université Côte d’Azur.

References

- [1] C. T. January, L. S. Wann, H. Calkins, J. E. Cigarroa, *et al.*, “2019 AHA/ACC/HRS focused update of the 2014 AHA/ACC/HRS guideline for the management of patients with atrial fibrillation,” *Journal of the American College of Cardiology*, vol. 74, no. 1, pp. 104–132, 2019.
- [2] L. Mainardi, L. Sörnmo, and S. Cerutti, *Understanding Atrial Fibrillation: The Signal Processing Contribution*. Morgan & Claypool Publishers, 2008.
- [3] J. J. Rieta, F. Castells, C. Sánchez, V. Zarzoso, and J. Millet, “Atrial activity extraction for atrial fibrillation analysis using blind source separation,” *IEEE Transactions on Biomedical Engineering*, vol. 51, no. 7, pp. 1176–1186, 2004.
- [4] L. De Lathauwer, “Blind separation of exponential polynomials and the decomposition of a tensor in rank- $(l_r, l_r, 1)$ terms,” *SIAM Journal on Matrix Analysis and Applications*, vol. 32, no. 4, pp. 1451–1474, 2011.
- [5] V. Zarzoso, “Parameter estimation in block term decomposition for noninvasive atrial fibrillation analysis,” in *IEEE 7th Int. Workshop Comput. Adv. Multi-Sensor Adapt. Process. (CAMSAP)*, Curaçao, Dutch Antilles, Dec. 2017.
- [6] P. M. R. de Oliveira and V. Zarzoso, “Block term decomposition of ECG recordings for atrial fibrillation analysis: Temporal and inter-patient variability,” *Journal of Communication and Information Systems*, vol. 34, pp. 111–119, 2019.
- [7] P. Kirchhof and H. Calkins, “Catheter ablation in patients with persistent atrial fibrillation,” *European Heart Journal*, vol. 38, no. 1, pp. 20–26, Jul. 2016.
- [8] M. Haïssaguerre, P. Jaïs, D. C. Shah, A. Takahashi, M. Hocini, *et al.*, “Spontaneous initiation of atrial fibrillation by ectopic beats originating in the pulmonary veins,” *New England Journal of Medicine*, vol. 339, no. 10, pp. 659–666, 1998.
- [9] J. Seitz, C. Bars, G. Théodore, S. Beurtheret, *et al.*, “AF ablation guided by spatiotemporal electrogram dispersion without pulmonary vein isolation: A wholly patient-tailored approach,” *Journal of the American College of Cardiology*, vol. 69, no. 3, pp. 303–321, 2017.
- [10] J. H. de M. Goulart, P. M. R. de Oliveira, R. C. Farias, V. Zarzoso, and P. Comon, “Alternating group lasso for block-term tensor decomposition and application to ECG source separation,” *IEEE Transactions on Signal Processing*, vol. 68, pp. 2682–2696, 2020.
- [11] M. Stridh and L. Sörnmo, “Spatiotemporal QRST cancellation techniques for analysis of atrial fibrillation,” *IEEE Transactions on Biomedical Engineering*, vol. 48, no. 1, pp. 105–111, 2001.
- [12] M. Yuan and Y. Lin, “Model selection and estimation in regression with grouped variables,” *Journal of the Royal Statistical Society: Series B (Statistical Methodology)*, vol. 68, no. 1, pp. 49–67, 2006.
- [13] J. A. Cadzow, “Signal enhancement-a composite property mapping algorithm,” *IEEE Transactions on Acoustics, Speech, and Signal Processing*, vol. 36, no. 1, pp. 49–62, 1988.
- [14] P. M. R. de Oliveira and V. Zarzoso, “Source analysis and selection using block term decomposition in atrial fibrillation,” in *14th International Conference on Latent Variable Analysis and Signal Separation (LVA/ICA)*, Guildford, UK, Jul. 2018, pp. 46–56.
- [15] V. Zarzoso and P. Comon, “Robust independent component analysis by iterative maximization of the kurtosis contrast with algebraic optimal step size,” *IEEE Transactions on Neural Networks*, vol. 21, no. 2, pp. 248–261, 2010.

Address for correspondence:

Pedro Marinho R. de Oliveira
Les Algorithmes, Euclide B, 2000 route des lucioles,
06900 Sophia Antipolis Cedex, France
marinho@i3s.unice.fr

Low-Rank Hankel Signal Model: Numerical Results

Lucas Abdalah, Walter Freitas Jr, Pedro Marinho R de Oliveira, Vicente Zarzoso

Abstract—Hankel matrices arise in several applications of signal processing, such as tensor decompositions, biomedical signal processing, etc. In general, these techniques rely on digital signals that can be modeled as a linear combination of exponential polynomials. Hence, the Hankel matrix built from these signals presents full rank, equal to the number of poles, ensured under mild constraints. The present work observes other features of the low-rank Hankel model, using singular value decomposition (SVD) to assess rank deficiency. The effects observed may impact blind source separation (BSS) problems.

Keywords—Vandermonde Decomposition, Hankel Matrix, Singular Value Decomposition, Low-Rank.

I. INTRODUCTION

One of the challenges in signal processing is the estimation of a set of source signals based on the observation of a set of mixed signals. A blind source separation (BSS) approach can be applied aiming to isolate the source signals and usually relies on matrix decompositions. Nevertheless, strong mathematical constraints are necessary to assure uniqueness of the decomposition, such as mutual orthogonality between spatial factors and statistical independence [1], [2]. The best-known matrix methods are based on principal and independent component analysis. In order to overcome these limitations, tensor decompositions are powerful tools, ensuring uniqueness and outperforming matrix-based methods under milder constraints [3].

A celebrated tensor-based method is the block term decomposition (BTD) [4], [5]. This technique takes advantage of discrete-time signals that can be modeled as linear combinations of exponentials (all-pole models). Since the sources can be expressed as low-rank Hankel matrices, the signal separation can be performed via BTD. The Hankel matrix built from such source signals accepts the Vandermonde decomposition [6], a well-known result in problems of matrix analysis and telecommunications. Different fields in signal processing take advantage on low-rank Hankel source models for speech analysis [7], black-box polynomial analysis [8], and tensor decompositions [4], some applied to biomedical signal analysis [5], [9].

The theoretical baseline relies on a strong assumption: since a Vandermonde matrix generated by distinct poles has full rank equal to the number of poles [4], the Hankel matrix mapped from a finite signal with enough samples presents its rank equal to the number of poles. This notion can be used to assess

Lucas Abdalah and Walter Freitas Jr are with Universidade Federal do Ceará, Wireless Telecom Research Group, Fortaleza-CE, {lucas.abdalah, walter}@gtele.ufc.br; Pedro Marinho R de Oliveira is with BioSerenity, Paris, France, pedro.marinho@bioserenity.com; Vicente Zarzoso is with Université Côte d'Azur, CNRS, I3S Laboratory, Sophia Antipolis, France, vicente.zarzoso@univ-cotedazur.fr. This work was partially funded by the National Council for Scientific and Technological Development (CNPq).

signal complexity, since the more poles a signal contains, the more complex it can be considered. The rank of a matrix can be computed with a popular and reliable method based on the singular value decomposition (SVD), that considers the rank as the number of singular values larger than a tolerance parameter [10].

However, the present work shows that numerical features such as the distance between the poles that generate the signal may impact the computed rank. Aiming to observe clearly the behavior described, we propose three different experiments: 1) Vandermonde matrix built from two vectors, to illustrate how the distance between poles hampers the construction of a full-rank matrix, and consequently how it impacts the singular values and the Hankel matrix rank; 2) multiple signals with various distances between poles vs. the amount of samples necessary to obtain the Hankel matrix rank equal to the number of poles contained in the signal; 3) scenario using the previous framework but with noisy signals with different signal-to-noise ratio (SNR).

The rest of this work is structured as follow: Section II presents the problem statement, whereas numerical experiments are presented in Section III. The discussions and conclusions based on the experimental results are given in Sections IV and V, respectively.

II. PROBLEM STATEMENT

A. Low-Rank Hankel Model

Assume that if a discrete time signal $s(n)$ is a linear combination of L damped complex exponentials, say:

$$s(n) = \sum_{l=1}^L c_l z_l^n, \quad 0 \leq n \leq N-1 \quad (1)$$

where $c_l, z_l \in \mathbb{C}$, are coefficients and poles, respectively.

The sequence $s(n)$ can be mapped onto an $(M \times M)$ Hankel matrix denoted \mathbf{H}_s , where each sample is placed along the anti-diagonal of \mathbf{H}_s as shown in Fig. 1, with mapping function $\mathbf{H}_{s(i,j)} = s(i+j-1)$, for i th row, and j th column. We assume N is odd without loss of generality, hence:

$$M = \frac{N+1}{2}. \quad (2)$$

A major result in signal processing states that \mathbf{H}_s accepts the following Vandermonde decomposition [4], [6]:

$$\mathbf{H}_s = \mathbf{V}_s \mathbf{D} \mathbf{V}_s^\top \quad (3)$$

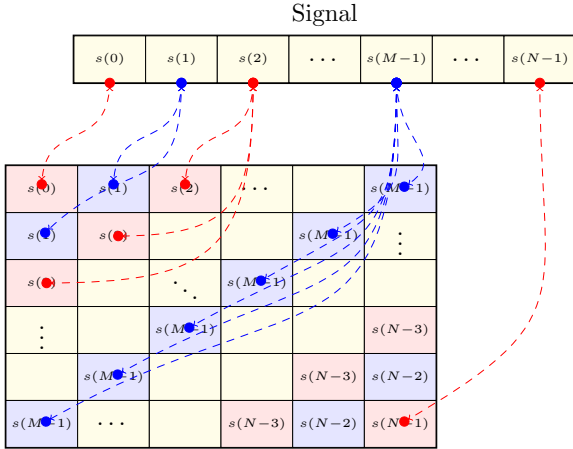


Fig. 1. Visual representation of a Hankel matrix \mathbf{H}_s built from a signal $s(n)$.

where \mathbf{V}_s is the Vandermonde matrix

$$\mathbf{V}_s = \begin{bmatrix} 1 & 1 & \dots & 1 \\ z_1 & z_2 & \dots & z_L \\ \vdots & \vdots & & \vdots \\ z_1^{M-1} & z_2^{M-1} & \dots & z_L^{M-1} \end{bmatrix} \in \mathbb{C}^{M \times L}, \quad (4)$$

and $\mathbf{D} = \text{diag}(c_1, c_1, \dots, c_L) \in \mathbb{C}^{L \times L}$ is a diagonal matrix. Symbol $(\cdot)^\top$ denotes the matrix transpose operator. We assume, for simplicity, but without loss of generality, that $c_l = 1$, $l = 1, 2, \dots, L$. As result of the Vandermonde decomposition (4), matrix \mathbf{H}_s has rank at most $\min\{L, M\}$. Hence, a first remark is that the more poles a given signal is composed of, the higher the rank of its Hankel matrix. This observation underlies the use of $\text{rank}(\mathbf{H}_s)$ as a measure of signal complexity. Nevertheless, a Hankel matrix build from a signal $s(n)$ with L poles needs to map at least N_{\min} samples:

$$N_{\min} = 2L - 1, \quad (5)$$

to present its rank R equal to L [4]–[6]. As soon as this minimum threshold is observed, the rank R should be equal to the number of poles L for a signal following model (1), regardless of the sample size.

B. Vandermonde Matrix and Pole Distance

When a signal is a sum of complex exponentials (1), its poles are closely linked to the columns of matrix \mathbf{V}_s , according to eqn. (4). If the distance between these poles decreases, the columns of \mathbf{V}_s become closer to each other, having an impact on the Hankel matrix rank.

To illustrate this behavior, we assume two poles $z_1 = e^{j\omega_1}$ and $z_2 = e^{j\omega_2}$, and the corresponding Vandermonde vectors $\mathbf{v}_1 = [1, e^{j\omega_1}, e^{j2\omega_1}, \dots, e^{j(M-1)\omega_1}]^\top$ and $\mathbf{v}_2 = [1, e^{j\omega_2}, e^{j2\omega_2}, \dots, e^{j(M-1)\omega_2}]^\top$.

We can observe that each vector norm is equal to M , where

$$\|\mathbf{v}_1\| = \|\mathbf{v}_2\| = M$$

and the columns scalar product leads to:

$$\mathbf{v}_1^\top \mathbf{v}_2 = \sum_{n=0}^{M-1} e^{-jn\omega_1} e^{jn\omega_2}.$$

Finally, replacing $\Delta\omega = (\omega_2 - \omega_1)$ and the exponential identities we have that the scalar product becomes:

$$\cos(\theta) = \frac{\mathbf{v}_1 \cdot \mathbf{v}_2}{\|\mathbf{v}_1\| \|\mathbf{v}_2\|} = \frac{\sin(M \frac{\Delta\omega}{2})}{M \sin(\frac{\Delta\omega}{2})}. \quad (6)$$

Based on the previous result, we can ensure that when $\Delta\omega$ tends to zero for a fixed M , we have that:

$$\lim_{\Delta\omega \rightarrow 0} \cos(\theta) = 1$$

showing that the columns becomes colinear, as expected, if the distance between poles ($\Delta\omega$) become too small. In this case, if we compare the singular values, the Hankel matrix rank is equal to one. This shows mathematically that a minimum distance between poles is required in practical scenarios. In this case, the equivalent Hankel matrix rank (R) is equal to one, built from two damped exponentials, resulting in $R \neq L$.

However, it is relevant to notice the presence of M in the denominator of eqn. (6). We can deduce that increasing the value of M used to build \mathbf{V}_s may compensate for the poles proximity. If we replace M using eqn. (2), we have that:

$$\cos(\theta) = \frac{2 \sin((N+1)\Delta\omega)}{(N+1) \sin(\frac{\Delta\omega}{2})}.$$

Therefore, for a small yet nonzero value of $\Delta\omega$, but nonzero, if we increase N then the scalar-product gets closer to zero (due to N in the numerator), in such a way that colinearity between \mathbf{v}_1 and \mathbf{v}_2 is reduced:

$$\lim_{N \rightarrow \infty} \frac{2 \sin((N+1)\Delta\omega)}{(N+1) \sin(\frac{\Delta\omega}{2})} = 0 \quad (7)$$

resulting in $R = L$, in agreement with the classical result observed in the literature [6].

C. Singular Value Decomposition

The SVD is a valuable tool in signal processing, a common technique for multivariate data analysis and provides a foundation for many other techniques such as principal component analysis (PCA) [11].

The SVD of $\mathbf{X} \in \mathbb{C}^{I \times J}$ is given by:

$$\mathbf{X} = \mathbf{U} \Sigma \mathbf{V}^H, \quad (8)$$

where $\mathbf{U} \in \mathbb{C}^{I \times I}$ and $\mathbf{V} \in \mathbb{C}^{J \times J}$ are unitary matrices with orthonormal columns, and the symbol $(\cdot)^H$ denotes the Hermitian operator. Diagonal matrix $\Sigma \in \mathbb{R}^{I \times J}$ contains real, non-negative entries. It can also be represented as $\Sigma = \text{diag}(\lambda_1, \lambda_2, \dots, \lambda_J)$, where each λ_j is a singular value, presented in decreasing order.

In order to compute the rank of \mathbf{X} , a reliable SVD-based method may be applied [12], [13]. It consists in performing $\text{SVD}(\mathbf{X})$, then taking the number of singular values $(\lambda_1, \dots, \lambda_J)$ that are larger than a tolerance $\varepsilon = \max(I, J) \|\mathbf{X}\| \mathcal{E}$, where \mathcal{E} is the minimum distance that the

floating point arithmetic can recognize between two numbers and $\|\mathbf{X}\|$ represents the frobenius norm of \mathbf{X} .

Another possible way to assess rank-deficiency is by the condition number (σ), taking advantage of the relationship between singular values. The criterion used in this work is the equation:

$$\sigma = \frac{\lambda_{\max}}{\lambda_{\min}} \quad (9)$$

that provides a quotient between its maximum and minimum singular values, respectively. A large condition number is linked to a matrix close to rank-deficiency.

III. EXPERIMENTAL RESULTS

The experiments are divided in 3 parts. The first and second parts consider noiseless signals, whereas the third part is on noisy signals. In the first part we build a Vandermonde matrix from two vectors to illustrate how the distance between poles in the vector hamper the construction of a full-rank matrix, and consequently how it impacts the condition number, as theoretically anticipated in sec. II-B.

In the second part, we test various distances between poles to assess the minimum amount of samples necessary to obtain the Hankel matrix rank equal to the number of poles contained in the signal.

Finally, in the third scenario noisy signals are analyzed with various SNR values.

A. Condition Number

We assess the relationship between the condition number (σ) and the number of samples (N) varying the distance between the poles ($\Delta\omega$). An example inspired on the theoretical problem statement is assuming two vectors \mathbf{v}_1 and \mathbf{v}_2 as presented in Section II-B, with $\omega_1 = 0$, and $\omega_2 = \Delta\omega$, *i.e.*, $\mathbf{v}_1 = [1, 1, 1, \dots, 1]^\top$ and $\mathbf{v}_2 = [1, e^{j\Delta\omega}, e^{j2\Delta\omega}, \dots, e^{j(M-1)\Delta\omega}]^\top$, where \mathbf{v}_1 and \mathbf{v}_2 are the columns of the Vandermonde matrix \mathbf{V}_s . Hence, the Hankel matrix $\mathbf{H}_s \in \mathbb{C}^{N \times N}$ associated with this model is built from a simplified form of eqn. (3), where $\mathbf{V}_s \in \mathbb{C}^{N \times 2}$ and $\mathbf{D} \in \mathbb{R}^{2 \times 2}$ is an identity matrix. After constructing the Hankel matrix, we compute the $\text{SVD}(\mathbf{H}_s)$ for 10 different values of N , rounding logarithmically spaced values in the interval $[10^1, 10^2]$, and considering 7 different values of $\Delta\omega$ as shown in Fig. 2.

In the first place, if the distances between poles are so small, then even increasing the number of samples, σ keeps very high. This behavior affects rank computation and may prevent us to obtain $R = L$. Fig. 2 also shows that σ decreases as we increase the number of samples to the columns, which compensates for the poles proximity as expected from the analysis of Section II-B.

Moreover, for $\Delta\omega = [8.91 \times 10^{-9}, 1.96 \times 10^{-9}]$, σ indicates that $\lambda_1 \gg \lambda_2$ for all values of N , but it presents $R \neq L$ until reaching enough samples. Nevertheless, as N increases, σ tends to 1, *i.e.*, the number of samples compensates for the insufficient distance between poles, allowing us to find $R = L$.

Finally, for other values of $\Delta\omega$, the condition number still indicates $\lambda_1 \gg \lambda_2$. However, with very few samples it is possible to find the rank (R) of \mathbf{H}_s equal to the number of

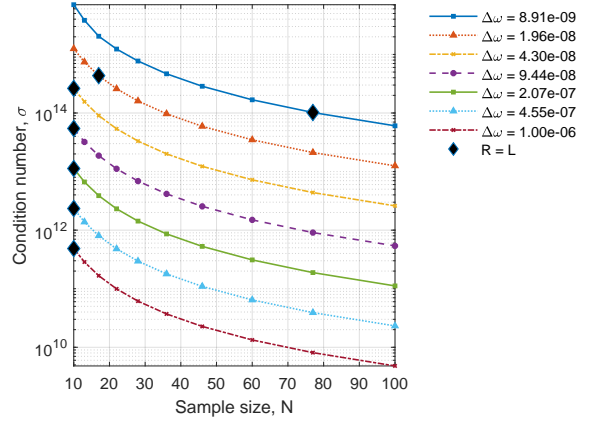


Fig. 2. Computing the condition number (σ) vs. the number of samples (N) to build the matrix using different values of $\Delta\omega$. For each curve, the diamond marker indicates the minimum value of N to have $\text{rank}(\mathbf{H}_s) = 2$.

poles L . It indicates that these are sufficient distances between poles.

B. Sample Size for a Full-Rank Hankel Matrix

This scenario aims to assess how the poles proximity ($\Delta\omega$) in a signal $s(n)$ with L poles, shown in eqn. (1), impacts its Hankel matrix rank R in the absence of noise.

The experiment consists in constructing \mathbf{H}_s from 100 samples for each $s(n)$. To compare the numerical and theoretical results, we use a windowed version of $s(n)$ with $N \leq 100$ samples to build its equivalent Hankel structure, *i.e.*, just the window $s(1:N)$ from the first N samples, is used to map the signal onto the matrix. Then, we search through each \mathbf{H}_s mapped from the windowed signal for the first value of N yielding $R = L$.

We generate $s(n)$, where z_l represent equispaced poles, L is in the $[2, 8]$ interval, and distance $\Delta\omega$ takes 100 logarithmically spaced values in the $[10^{-4}, 10^{-1}]$ interval. The number of samples used in window N is a positive integer value between 2 and 100. The simulation of Fig. 3 may be summarized as follows. For each value of L in the set of positive integers, we vary $\Delta\omega$ from very close poles gradually moving them away from each other at each iteration, noting the value of N for $R = L$.

The experiment shows that the theoretical values based on eqn. (5) are different from those obtained empirically. One would expect plots with horizontal lines at $2L - 1$ regardless of $\Delta\omega$. Nevertheless, the simulation presents a different result: when the distance gets smaller, the number of samples N necessary in the windowed signal to build \mathbf{H}_s with $R = L$ increases. This outcome reinforces the hypothesis that the increase of N may compensate for the distance between poles to obtain $R = L$ as anticipated by the analysis of Section II-B. This will increase the computational cost, since a reliable SVD algorithm (Golub-Reinsch) performs $8M^3/3$ flops to compute only the singular values [12], where M is the matrix dimension following eqn. (2).

Furthermore, one can see that as L increases, the curves move towards top right corner of the figure, which suggests

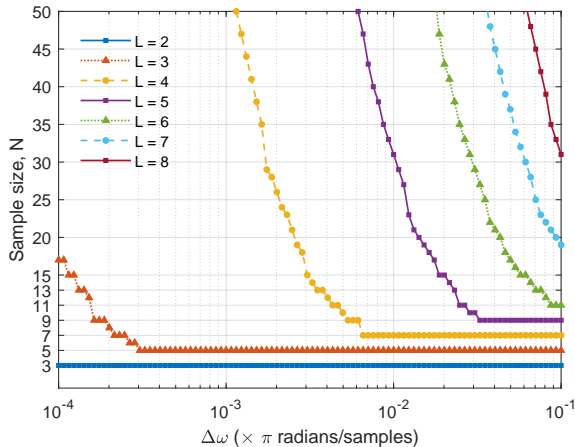


Fig. 3. Number of samples N necessary to build a Hankel matrix \mathbf{H}_s , with $R = L$, versus the distance between poles ($\Delta\omega$). variation.

that rank depends on number of poles and $\Delta\omega$.

C. Noisy Scenario and SNR Threshold

To assess a more realistic case, one may consider a scenario with additive white Gaussian noise (AWGN), according to the following data model:

$$y(n) = s(n) + \beta(n). \quad (10)$$

The simulation framework setup is similar to the presented in Section III-B, except for the mapped signal $y(n)$, a version of $s(n)$ as shown in eqn. (1), affected by the AWGN term $\beta(n)$, and with a fixed distance between poles $\Delta\omega = 0.05$.

Aiming to compare the theoretical values based in eqn. (5) with the data obtained empirically, we present an experiment that varies high SNR values, along the [250,320] interval in 10 dB steps. The experiment is performed to search a threshold SNR value, where the equivalent Hankel matrix \mathbf{H}_s presents a rank R equal to the number of exponentials L , regardless of $\Delta\omega$. We repeat the procedure described in Section III-B (Fig. 3) for each SNR, and noting the results obtained for each single run. The scenario with 100 Monte Carlo runs is computed varying the noise for each realization.

Fig. 4 shows that for values of SNR less than 270 dB, in general the most commonly encountered in real problems, the theoretical result is respected. The plots illustrate the expected result, discussed in previous sections, with horizontal lines at $2L - 1$, despite the $\Delta\omega$ variation with a rank R dependent only on its number of poles. For values greater than 270 dB, the theoretical values are once again different from those obtained empirically, but N starts to increase.

Finally, for this case of study, the three largest values of L present a transition close to 290 dB. We can see that for higher values of SNR, the trend observed in Fig. 3 at $\Delta\omega = 0.05$ is exactly the same for all L . This outcome supports the results of Section III-B, obtained in the noiseless case.

IV. DISCUSSION

The present work discusses the numerical features of the low-rank Hankel signal model using Vandermonde decompo-

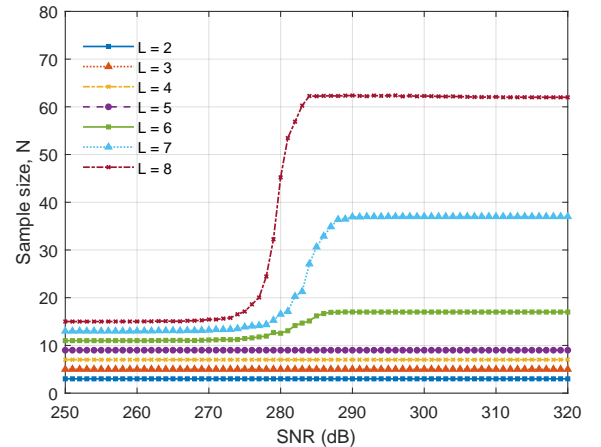


Fig. 4. Number of samples N necessary in the windowed signal $y(n)$ to build \mathbf{H}_s , with $R = L$, versus the SNR values, and fixed distance between poles $\Delta\omega = 0.05$ for 100 Monte Carlo runs.

sition. It explores various parameters as the distance between poles, and number of poles and samples in the construction of Hankel structures, mapped from all-pole signals.

Experiments based on the SVD measure the impact of parameters, taking into consideration two indices: the condition number, and the amount of samples mapped onto a Hankel matrix necessary to present a rank equal to the number poles in the equivalent signal. An unexpected relationship between the parameters appears in the noiseless case due to numerical effects, despite the noisy setup that presents the expected behavior with a limited SNR. Also, evidence was given with the help of simulations to support two remarks:

- (I) As the distance between poles decreases, the number required to obtain a full rank matrix increases. Furthermore, in the second noiseless scenario, with a low-rank Hankel signal model, if the poles get too close to each other, a dependency between the rank, number of poles, amount of samples, and the distance between poles is observed.
- (II) In the noisy scenario, with SNR values commonly encountered in practice, the distance between poles becomes irrelevant. The theoretical minimum value is observed, *i.e.*, the rank depends only on the number of poles.

V. CONCLUSION AND FURTHER WORK

This work has studied the numerical features of Hankel matrices associated with complex exponential signal models. In the noiseless cases, to assure a full rank matrix and avoid the numerical problems presented, a minimum distance between poles is required or the number of mapped samples must increase to compensate for pole proximity and ensure full rank. These observations may impact the computational cost where the Vandermonde decomposition and Hankel structure are applied. In the noisy case, in real applications: with a realistic noise level, the Hankel matrix is always full rank, since the noise acts to balance the linear independence between the columns in the associated Vandermonde matrix. This can

reduce significantly the computational cost for problems with solid ground-truth.

Future work should focus on performing the condition number experiment for larger Vandermonde matrices, in order to compare more than two singular values to provide more relevant statistical information. Furthermore, the experiments should be in the context of tensor decompositions, such as BTD, since the model performs the separation of the noise in a different block of the low-rank Hankel signal model and the remaining blocks could fall within the noiseless scenario.

ACKNOWLEDGMENT

Lucas Abdalah is supported by CNPq (Conselho Nacional de Desenvolvimento Científico e Tecnológico) within the Ministry of Science and Technology of Brazil.

REFERENCES

- [1] V. Zarzoso, “Extraction of ECG characteristics using source separation techniques: Exploiting statistical independence and beyond,” in *Advanced Biosignal Processing*, A. Nait-Ali, Ed., Springer, 2009, ch. 2, pp. 15–47.
- [2] V. Zarzoso and P. Comon, “Robust independent component analysis by iterative maximization of the kurtosis contrast with algebraic optimal step size,” *IEEE Transactions on Neural Networks*, vol. 21, no. 2, pp. 248–261, 2010.
- [3] P. M. R. de Oliveira and V. Zarzoso, “Block term decomposition of ecg recordings for atrial fibrillation analysis: Temporal and inter-patient variability,” *Journal of Communication and Information Systems*, vol. 34, no. 1, pp. 111–119, 2019.
- [4] L. De Lathauwer, “Blind separation of exponential polynomials and the decomposition of a tensor in rank- $(L_r, L_r, 1)$ terms,” *SIAM Journal on Matrix Analysis and Applications*, vol. 32, no. 4, pp. 1451–1474, 2011.
- [5] J. H. de M. Goulart, P. M. R. de Oliveira, R. C. Farias, V. Zarzoso, and P. Comon, “Alternating group lasso for block-term tensor decomposition and application to ECG source separation,” *IEEE Transactions on Signal Processing*, vol. 68, pp. 2682–2696, 2020.
- [6] D. Boley, F. Luk, and D. Vandevoorde, “A general Vandermonde factorization of a Hankel matrix,” *Int. Lin. Alg. Soc.(ILAS) Symp. on Fast Algorithms for Control, Signals and Image Processing*, 1997.
- [7] L. Weruaga and A. Al-Khayat, “All-pole model estimation of vocal tract on the frequency domain,” *Proceedings of the Annual Conference of the International Speech Communication Association*, vol. 2, 2006.
- [8] B. Beckermann, G. Golub, and G. Labahn, “On the numerical condition of a generalized Hankel eigenvalue problem,” *Numerische Mathematik*, vol. 106, pp. 41–68, 2007.
- [9] L. Abdalah, P. M. R. de Oliveira, W. Freitas, and V. Zarzoso, “Tensor-based noninvasive atrial fibrillation complexity index for catheter ablation,” in *Computing in Cardiology*, Rimini, Italy, Sep. 2020.
- [10] Z. Drmac, “SVD of Hankel matrices in Vandermonde-Cauchy product form,” *Electronic Transactions on Numerical Analysis*, vol. 44, pp. 593–623, 2015.
- [11] M. E. Wall, A. Rechtsteiner, and L. M. Rocha, “Singular value decomposition and principal component analysis,” in *A Practical Approach to Microarray Data Analysis*, D. Berrar, W. Dubitzky, and M. Granzow, Eds. 2003, pp. 91–109.
- [12] G. H. Golub and C. F. van Loan, *Matrix Computations*, Fourth ed. John Hopkins University Press, 2013.
- [13] S. L. Brunton and J. N. Kutz, “Singular value decomposition (SVD),” in *Data-Driven Science and Engineering: Machine Learning, Dynamical Systems, and Control*. Cambridge University Press, 2019, pp. 3–46.